

Role of the Aortic Arch in Idiopathic Unilateral Vocal Fold Paralysis

by

Seyyed Reza Behkam

Mechanical Engineer, Sharif University of Technology, Iran, 2004

Master of Science in Mechanical Engineering, Sharif University of
Technology, Iran, 2011

Master of Science in Mechanical Engineering, University of Arizona,
2016

Submitted to the Graduate Faculty of
the Swanson School of Engineering in partial fulfillment
of the requirements for the degree of

Doctor of Philosophy

University of Pittsburgh

2019

UNIVERSITY OF PITTSBURGH
SWANSON SCHOOL OF ENGINEERING

This dissertation was presented

by

Seyyed Reza Behkam

It was defended on

September 30, 2019

and approved by

Jonathan Vande Geest, Ph.D., Professor, Department of Bioengineering

Julie Barkmeier-Kraemer, Ph.D., Professor, Division of Otolaryngology - Head & Neck

Surgery, University of Utah

Steven Abramowitch, Ph.D., Associate Professor, Department of Bioengineering

Alejandro Almarza, Ph.D., Associate Professor, Oral Biology, School of Dental Medicine

Dissertation Director: Jonathan Vande Geest, Ph.D., Professor, Department of

Bioengineering

Copyright © by Seyyed Reza Behkam
2019

Role of the Aortic Arch in Idiopathic Unilateral Vocal Fold Paralysis

Seyyed Reza Behkam, PhD

University of Pittsburgh, 2019

Vocal fold paralysis is the most common neurogenic disorder of the larynx, which is associated with impaired swallowing, voice production, and breathing. There are various etiologies for vocal fold paralysis, including malignancy, trauma, iatrogenic surgical injuries and idiopathic. Impaired function of the recurrent laryngeal nerve (RLN) is known to be the primary cause of unilateral vocal fold paralysis (UVP). The RLNs on both sides are closely interacting with the cardiovascular system. Specifically, the left RLN originates from the vagus nerve, loops underneath the arch and ascends toward the larynx. Due to the proximity of the RLN to the aortic arch, one possible cause of damage to the left RLN may be associated with the supraphysiological forces imposed on the nerve by the aortic arch. In this dissertation, we investigated an association between the left-sided idiopathic unilateral vocal fold paralysis (iUVP) and the biomechanical behavior of the aortic arch. We studied the compliance of the aortic arch in a group of iUVP patients and age-gender matched controls. The results showed that the aortic arch is hypercompliant in iUVP patients. As the compliance variation might originate from differences in the aortic arch material properties, we utilized an inverse finite element approach to characterize the *in vivo* mechanical properties of the aortic wall. We showed that the matrix and fiber stiffness values are significantly lower in the iUVP patients. In the last stage of this work, we utilized a porcine model to study the microstructure of the RLN connective tissue under mechanical insult. Our study showed that the RLN biomechanical response under compression is a function of anatomical location and animal age. In conclusion, this work advanced our understanding of a possible iUVP etiology related to the cardiovascular system. Furthermore, our study suggested that RLN connective tissues develop in response to the environmental forces to preserve the integrity of the axons under various loading conditions. Also, the proposed computational framework based on the *in vivo* information can be used to investigate the pivotal role of the aortic arch biomechanics as it relates to the onset and development of other cardiovascular diseases.

Table of Contents

Preface	ix
1.0 Introduction	1
1.1 Vocal Fold Paralysis and Recurrent Laryngeal Nerve	1
1.2 Hypotheses and Specific Aims	3
2.0 Specific Aim 1 Aortic Arch Compliance in Idiopathic Unilateral Vocal Fold Paralysis Patients	5
2.1 Introduction	5
2.2 Methods	6
2.2.1 Study Population	6
2.2.2 Imaging Protocol	7
2.2.3 Measurements	8
2.2.4 Statistical Analysis	10
2.3 Results	11
2.4 Discussion	14
2.5 Conclusion	16
3.0 Specific Aim 2 Determination of the Aortic Arch Mechanical Properties for iUVP Patients and Controls Using <i>in vivo</i> Data	17
3.1 Introduction	17
3.2 Methods	18
3.2.1 Study Population & Imaging Protocol	18
3.2.2 Image Processing and Geometry Creation	19
3.2.3 Displacement Field Calculation	19
3.2.4 Finite Element Model and Optimization	20
3.2.5 Statistical Analysis	24
3.3 Results	24
3.4 Discussion	27

3.5 Conclusion	32
4.0 Specific Aim 3 Extracellular matrix deformations of the porcine recurrent laryngeal nerve in response to compression	33
4.1 Introduction	33
4.2 Methods	35
4.2.1 Sample Acquisition and Preparation	35
4.2.2 Compression Test and Imaging	36
4.2.3 Displacement and Strain Calculation	38
4.2.4 Histological Study	39
4.2.5 Statistical Analysis	40
4.3 Results	40
4.4 Discussion	43
5.0 Discussion	47
5.1 Overview	47
5.2 Summary of Results	48
5.2.1 Chapter 2: Compliance Variation Across iUVP Patients and Healthy Subjects	48
5.2.2 Chapter 3: Specific Aim 2 Determination of the Aortic Arch Mechanical Properties for iUVP Patients and Controls Using <i>in vivo</i> Data	49
5.2.3 Chapter 4: Extracellular matrix deformations of the porcine recurrent laryngeal nerve in response to compression	49
5.3 Limitation and Future Work	50
5.4 Dissertation Conclusions	52
Bibliography	54

List of Figures

1	A) Anatomy of the RLN. B) A Sagittal view of the human aorta.	9
2	A) 3D reconstructed aorta with the computed centerline and a schematic view of the cutting plane (ϕ). B: The dashed red line is the result of the intersection between one slice of the image stack and the plane (ϕ) to calculate the first angle of rotation. C) The rotated image after the first rotation in XY plane on one sagittal slice.	10
3	A: An aorta segmented area on a plane normal to centerline close to brachiocephalic root B: The least square ellipse fit to the segmented area C: The aortic centerline and selected cross section close to brachiocephalic branch for maximum and minimum aortic diameter	11
4	Diameter of a brachiocephalic segment of the aorta for a healthy female, 53 yrs. old	12
5	Pressure pulse for all age groups * : post hoc p-value for young and middle age group is 0.046 , **: post hoc p-value for young and old age group is 0.008	12
6	Aortic arch diameter change in healthy people is significantly smaller than iUVP patients (p=0.04)	13
7	Mean compliance as a function of age and disease. Post hoc p-value between all the age groups are smaller than 0.005	14
8	A) The reconstructed geometry was cut normal to the aorta centerline, and then an ellipse was fitted to each cross-section.(α) shows the location of the brachycephalic artery B) The geometrical model was created by performing a 3D loft using the elliptical cross-sections and centerline.	20
9	A) Mesh independency study for the arch model B) S3R elements were used to mesh the aortic arch.	22
10	Wall thickness was defined as a function of age.	24
11	Utilization of the 6 cores resulted in the optimum computational cost	25

12	Age group and disease were significant effects for the stiffness of the matrix. C_{10} was smaller in the old iUVP group compared to the same age group of the controls (p-value = 0.035)	26
13	Fiber stiffness (K_1) increased significantly with age in iUVP subjects and controls. It was also greater in the control group than the iUVP group within the old age group (p-value=0.047)	27
14	Age group and disease were significant effects for the fiber stiffness parameter. It was significantly smaller in the old iUVP group than the old control subjects (p-value= 0.032).	28
15	Age group was the only significant effect for the percentage shrinkage parameter.	29
16	Left and right RLN of an adolescent porcine	36
17	A) compression chamber was designed to maintain hydrostatic pressure up to 80 mmHg. B) A Cartesian coordinate system was defined to investigate specimen strain field. C) The nerve specimen was glued to a coverslip. SHG Imaging was performed at the center point of the sample under compression.	37
18	A) Experimental setup under the multiphoton microscope to collect SHG signals. B) Mean intensity projection of a representative left RLN from a piglet at 0 mmHg.	38
19	Strain component in the axial direction (E_{xx}) averaged through the thickness (z-axis) for the distal section of a right piglet RLN at the first pressure increment	41
20	Strain metrics for the left distal segment of the RLN as a function of animal age and pressure level A) Median of the E_{ps1} was significantly higher in pigs compared to piglets at the first pressure increment. Also, it was higher in pig group at the first pressure increment compared to the second pressure increment. B) 95 th percentile of the 1st principal strain showed a similar trend as the median of the E_{ps1}	42
21	At the second pressure increment and for the proximal segment of RLN, the median of E_{yy} across the pig group was significantly larger than the left side. Also, it was greater in the pig right RLN compared to the right piglet RLN. .	43
22	Distribution of the collagen fiber orientation at 0 and 80 mmHg	44

Preface

This dissertation would not have been possible without the guidance of my professors, support of my friends, and the love from my family. I express my thanks to those who supported me for my graduate research and study. I am grateful to Drs. Jonathan Vande Geest, Julie Barkmeier-Kraemer, Steven Abramowitch and Alejandro Almarza for serving on my committee. I would like to especially thank my advisor, Dr. Jonathan Vande Geest, for his constructive guidance, advice, and encouragement during this research that words cannot explain. He constantly encouraged me in every step of the way and without his guidance this journey would not be possible. The knowledge and the passion he has provided me with goes beyond what I can get from any other sources.

I especially thank my wife, Sara Minaeian, for her love and understanding. She has been extremely supportive throughout this journey and has made countless sacrifices to help me get to this point.

I would like to thank all the former and current faculty and staff members of the Department of Bioengineering. I would like to especially thank Dr. Sanjeev Shroff for his support. I extend my thanks to all former and current members of the soft tissue biomechanics laboratory (STBL) especially Megan Williams, Avinash Ayyalasomayajula, Hirut Kollech, Ali Behrangzade, Kenny Furdella, Jr Jiun Liou, Ehab Tamimi and Catalina Ardila for their untiring enthusiasm and patient help in the course of my research work.

Last but not the least, I would like to thank my entire family and friends, especially my beloved parents Maryam and Asad Behkam, my lovely sisters Razieh and Bahareh, and my awesome in-laws for providing a loving environment and for believing in me.

I dedicate this dissertation to:

My parents, Maryam and Asad Behkam, who bore me, raised me, supported me, taught me, and loved me.

My brilliant and outrageously loving and supportive wife, Sara Mianeian, who encouraged me to pursue my dreams.

1.0 Introduction

The recurrent laryngeal nerve (RLN) is the primary motor supply to the muscles of the vocal folds in the larynx that are important for protection of the airway during swallowing, breathing, and speaking. Thus, paralysis or paresis of one of the vocal folds, such as with unilateral vocal fold paralysis/paresis (UVP), often results in impaired voicing, breathing, or swallowing safety [28, 32, 48]. Among those diagnosed with UVP, 38% exhibit aspiration during swallowing due to the impaired closure of the larynx necessary to protect the airway during eating [46].

1.1 Vocal Fold Paralysis and Recurrent Laryngeal Nerve

The vocal folds play a key role in the protection of the airway during swallowing, regulation of breathing and voice production. Unilateral vocal fold paralysis (UVP) occurs when the recurrent laryngeal nerve (RLN) is damaged. The RLN supplies all of the muscles of the larynx excluding the cricothyroid muscles. The right and left RLNs exhibit asymmetrical lengths and pathways due to differing locations of vagus nerve branching. The right RLN branches from the vagus nerve at the level of the subclavian artery before traveling around the underside of this vessel and ascending to the larynx between the trachea and esophagus. In contrast, the left RLN bifurcates from the vagus nerve within the thorax near the aortic arch and courses adjacent to the underside of the aorta before ascending toward the larynx within the tracheoesophageal groove (Figure 1A) [44, 75, 78]. A recent evaluation of UVP patient characteristics showed that vocal fold paralysis affects the left side in approximately 2/3 of individuals [105]. Demographic reports vary only slightly in the proportion of males and females presenting with unilateral vocal fold paralysis. Slightly more females than males exhibited UVP in the cohort reported by Sparato et al. [105] whereas Kelchner et al. [54] and Loughran et al. [64] reported slightly more males than females. In general, the average age of UVP onset is reported to be near 50 years of age or older [105, 54, 110].

UVP etiologies include iatrogenic, neoplasm, respiratory infections, and idiopathic (i.e. unknown cause) [105, 54, 110, 77, 115, 23, 94]. One of the larger UVP etiology groups is the idiopathic etiology [105, 110]. One potential source of idiopathic RLN injury may be that of a viral neuropathy [18, 16, 7]. Support for this hypothesis comes primarily from case-based publications reporting the association of idiopathic bilateral and unilateral vocal fold paralysis associated with upper respiratory infection or viral infections [105, 7, 36, 88, 107, 33]. However, a viral etiology offers equal opportunity to affect the left and right RLNs [105, 110]. Yet, injury to the left RLN represents the majority of those diagnosed with the idiopathic onset of UVP. Thus, the preponderance of idiopathic UVP affecting the left RLN requires an alternative explanation consistent with idiopathic population characteristics.

Interestingly, left-sided RLN can be associated with a myriad of cardiothoracic conditions [105, 54, 110, 115, 23, 76] such as lung cancer, thoracic surgery, tumors, neck, chest or cardiovascular lesions and edema [78, 30, 53]. Several case-based studies suggest that the extended course of the left RLN through the thoracic cavity potentially exposes the nerve to damaging forces associated with compression and stretch from adjacent pulsating anatomical structures such as the pulmonary arteries, aorta, and left atrium. Stocker et al. first ascribed the association of hoarseness and cardiovascular pathology as cardio vocal syndrome in 1958 [109]. Ortner also reported hoarseness of the voice due to left RLN paralysis in patients with mitral stenosis [83]. Dolowitz et al. reported that the LRLN could be compressed by the pulmonary artery, aortic arch, and ligamentum arteriosum because of cardiac hypertrophy and pulmonary artery engorgement [30]. Changes in vascular diameter at the location of the RLN (i.e. aneurysm) can also affect left-sided RLN function. Pressler et al. reported the emergence of cardiovocal syndrome in 5% of patients with a thoracic aneurysm and left RLN paralysis [89]. Aneurysm of the aorta and pulmonary artery [34], or a ductal aneurysm [27], was also linked with the onset of left RLN damage. Other cardiovascular diseases such as a thrombosed giant left atrium [91], mitral stenosis [83], and arterial myxoma [97] have also been associated with the onset of left RLN paralysis. These examples highlight the interaction between cardiothoracic tissues, particularly larger pulsatile vessels such as the aortic arch and pulmonary artery, and the left RLN suggesting the vascular system as a potential factor for consideration.

One study modeled the level of stress and strain imparted by the aortic arch onto the RLN using a finite element analysis approach. A strong correspondence occurred between aorta conditions and stress and strain levels of the left RLN suggesting a link between aortic conditions and RLN tissue mechanics [122]. These findings were also of great interest in the context of age-based vascular tissue changes. Specifically, aortic arch diameter significantly increases with every decade that passes [99] whereas compliance gradually decreases over time beyond the age of 10 years of age [57, 56]. Given the average age of onset of idiopathic RLN averaging 50 years or older, age-based changes in the aorta could play a role in the onset of left-sided UVP. Of specific interest is the possibility that age-related changes in the aorta might cause conditions of supraphysiological stretch and compression causing left RLN dysfunction [61, 74, 106]. Thus, abnormal age-related changes in the aorta could affect left-sided RLN function.

1.2 Hypotheses and Specific Aims

This thesis sought to further highlight the interactions between vascular compliance, particularly of the aortic arch, and the left RLN. The objective of this work was to quantify compliance and mechanical properties of the aortic arch in those with iUVP as well as develop an ex-vivo approach to further investigate how left RLN function depends on this great vessel. We believe this research will eventually lead to a better understanding of how variations in cardiovascular properties contribute to iUVP. The above objective was followed by testing the following three hypotheses:

Hypothesis 1: Individuals with idiopathic left-sided UVP will exhibit a greater aortic arch compliance than age-matched controls.

Specific Aim 1: Determine whether there are differences between gated MRI measures of aortic arch compliance between individuals diagnosed with left-sided idiopathic UVP and age-matched controls. *Rational:* Several case-based studies suggest that the extended course of the left RLN through the thoracic cavity potentially exposes the nerve to damaging forces

associated with compression and stretch from adjacent pulsating anatomic structures such as aortic arch. Supraphysiological levels of left RLN stretch due to the higher aortic arch compliance could contribute to iUVP.

Hypothesis 2: Aortic arch material properties are different in those with left-sided iUVP compared to age- and gender-matched controls.

Specific Aim 2: Determine the mechanical properties of the aortic arch in iUVP and age/gender matched controls using an inverse finite element model approach. The aortic arch geometry and displacement field will be extracted from the patient specific gated MRI images using a digital volume correlation technique and an automated inverse finite element approach will be used to determine the patient-specific aortic mechanical properties that minimize the residuals between the MRI and computational data. *Rationale:* Our research team has identified an increase in aortic compliance in iUVP patients compared to controls. Assuming there is no difference in aortic wall thickness, one potential cause of increased compliance in iUVP patients is a change in aortic wall mechanical properties.

Hypothesis 3: Hydrostatic pressures up to 80 mmHg cause an increased level of strain on the porcine RLN

Specific Aim 3: Determine strain in the porcine RLN generated due to imposed external fluid pressure around the entire nerve. The RLN will be secured in its in-vivo length and pressurized using a controlled pressure head. Incremental increases in fluid bath pressure will be imposed on the nerve from 0 to 80 mmHg in increments of 20 mmHg. Multiphoton images of collagen fiber organization and tissue strain will be quantified for each of the four pressure steps. *Rationale:* Edema due to surgery or other conditions can result in an increased fluid pressure on the RLN. It has also been suggested that epineurial blood flow can be halted beyond pressures of 60-80 mmHg [98]. We seek to identify when changes in epineurial collagen occur in response to externally applied pressure.

2.0 Specific Aim 1 Aortic Arch Compliance in Idiopathic Unilateral Vocal Fold Paralysis Patients

In this aim, I studied a potential source of RLN damage in iUVP patients. As left RLN loop around the aortic arch and travels toward the larynx, the connection between aortic arch compliance and presence of the iUVP was elevated to illustrate if the biomechanics of this large vessel (i.e. aorta) could originate any damage to the nerve. This aim focused on the determination of the aortic arch compliance across a group of iUVP patients and an age-gender match control group.

The results of this aim have been published in the Journal of Applied Physiology: **Behkam Reza**, Kara E. Roberts, Andrew J. Bierhals, M. Eileen Jacobs, Julia D. Edgar, Randal C. Paniello, Gayle Woodson, Jonathan P. Vande Geest, and Julie M. Barkmeier-Kraemer. "Aortic arch compliance and idiopathic unilateral vocal fold paralysis." Journal of Applied Physiology 123, no. 2 (2017): 303-309.

2.1 Introduction

As it was mentioned in section 1.1, abnormal cardiovascular system conditions were shown to be associated with iUVP onset and development. The purpose of this study was to compare aortic arch diameter and compliance between individuals diagnosed with left-sided idiopathic UVP and age- and gender-matched controls. Based on preliminary finite element estimates of aortic arch compliance levels and RLN tissue stress and strain values [122], it was hypothesized that significantly greater aortic arch compliance occurs in individuals with left-sided iUVP than normal controls.

2.2 Methods

2.2.1 Study Population

This study was approved by the Washington University, St Louis Institutional Review Board (IRB) (IRB Protocol #201206033). Participants recruited for this study were at least 21 years of age, and recruited from Washington University Medical Center Department of Otolaryngology and Volunteers for Health. All subjects were required to be free from conditions that would preclude undergoing MRI scanning and to be able to hold their breath for 10-20 seconds duration. Finally, due to the cardiac cycle gating of MR imaging, participants were excluded if diagnosed with cardiac arrhythmia at the time of the study. Two groups were recruited for comparison including individuals diagnosed with left-sided idiopathic vocal fold paralysis and age- and gender-matched controls.

Individuals diagnosed with left-sided idiopathic vocal fold paralysis were included if they were diagnosed within the previous five years and underwent laryngeal imaging and radiologic evaluation of the chest and neck to rule out other structural and disease abnormalities. Also, participants with left-sided idiopathic UVP did not have a history of surgery or diagnosis of neoplasm affecting aerodigestive, neural, or skeletal structures associated with the skull, spine, neck/throat, or cardiothoracic regions associated with the onset of the left-sided UVP. Individuals previously diagnosed with idiopathic left-sided UVP and spontaneous recovery within five years after diagnosis were also included given the goals of this study.

Individuals in the normal control group were age- and gender-matched to the disorder group and were recruited from a research volunteer service at Washington University who met inclusion criteria. For each iUVP participant completing the study, a normal age- and gender-matched control was recruited. Age matching was conducted so that each matched normal control was within +2 years of the associated idiopathic UVP participants age. Normal control volunteers meeting gender and age-matching criteria were excluded if they had a prior history of a voice problem associated with surgery, trauma, or neoplasm affecting the same structural regions applied to the disorder group. Also, they were excluded if diagnosed with a neurodegenerative disease or autoimmune disease known to affect connective tissues.

Twenty-two participants met inclusion criteria, 11 in each group (iUVP and Controls). Of these, the MR imaging data from 2 participants exhibited excessive noise and were excluded from analysis due to the inability to complete measures. The final participant group consisted of 13 female and seven male volunteers, averaging 53 years of age with a range from 26-82 years old.

2.2.2 Imaging Protocol

Aorta regional geometry images including the location of the left RLN near the brachiocephalic root were acquired using gated magnetic resonance (MR) imaging. Image acquisition was performed in the Department of Radiology, Washington University, St. Louis. MR scanning was completed using a 32-channel 1.5 Tesla MR Avanto (Seimens, Melvern, PA) scanner with a maximum gradient amplitude of 45 mT/m and maximum slew rate of 200 mT/m/ms along each physical axis. Images were acquired at a sampling rate of 25 Hz per heart cycle for each patient. Prior to the onset of MR scanning procedures, heart rate, and blood pressure measures were recorded with participants in the supine position. Once positioned for scanning, 3D segmented steady-state free-precession sequencing with nonselective radiofrequency excitation was implemented for image acquisition. Electrocardiogram (ECG)-gating with data acquisition during diastole and systole was also used to control for cardiac motion artifacts during image acquisition. The following imaging parameters were set: TR 2.3 milliseconds, TE 1.0 milliseconds, flip angle 90 degrees, readout bandwidth 980 Hz/pixel, FOV 400 - 400 mm², matrix size 256 - 256 leading to in-plane resolution of 1.6 - 1.6 mm². A total of 44 to 64 3D partitions were measured with a slice thickness of 1 mm interpolated to 88 to 128 slices of 1.5 mm. Fifty-one to 77 lines were measured during each cardiac cycle depending on the heart rate. To shorten the scan time, a parallel imaging technique, generalized autocalibrating partially parallel acquisition or GRAPPA, with an acceleration factor of 2, was applied. Data acquisition was obtained first using ungated MRI in the sagittal and axial orientations followed by gated FIESTA MRI scanning of the oblique, coronal, and axial orientations. Asymmetric data sampling of k-space with navigator acceptance rate of 30 to 60% was used resulting in a scan time of 15-20 minutes.

2.2.3 Measurements

Compliance was defined as the change in aortic diameter during a cardiac cycle normalized to pulse pressure [51]:

$$C = \frac{(d_{sys} - d_{dias})}{d_{dias}(P_{sys} - P_{dias})} \quad (2.1)$$

The larger the compliance, the less energy needed to create deformation. For example, subjects with higher aortic compliance show a bigger change in aortic diameter for the same one-unit change in pressure. The maximum systolic (d_{sys}) and minimum diastolic diameter (d_{dias}) of the aorta were derived from analysis of the gated MRI data. Sagittal view image stacks were taken such that the images enabled us to reconstruct aortic arch geometry in the 25-time points that cover one heart cycle. A sagittal view of the aorta for one iUVP patient is shown in Figure 1B.

The aorta was assumed to have an elliptical cross-section, and the average of the major and minor axes was defined as the cross-sectional diameter. Our research group investigated two approaches to measuring aortic diameter from MR images. The first approach was 3D reconstruction [9, 11] of the aorta followed by computation of diameter at the point of interest. The second approach was 2D image segmentation of the aorta at a cross section normal to the centerline of the aorta. The first approach was easier to implement using commercial software however difficulties arose related to the 3D reconstruction with respect to the error associated with surface smoothing. The maximum change in aortic diameter over a heart cycle for humans is usually less than 3 mm [57, 108]. Thus, any smoothing algorithm will increase error and potentially result in a miscalculation of the changes in diameter. To resolve this problem, an aortic centerline was computed [8, 87] and a plane (ϕ) was defined orthogonal to the centerline at the point of interest as illustrated in Figure 2A. Monfared et. al. [75] reported that the left RLN branches from the vagus nerve immediately posterior to the brachiocephalic vein and then runs anterolateral to the arch of the aorta. Therefore,

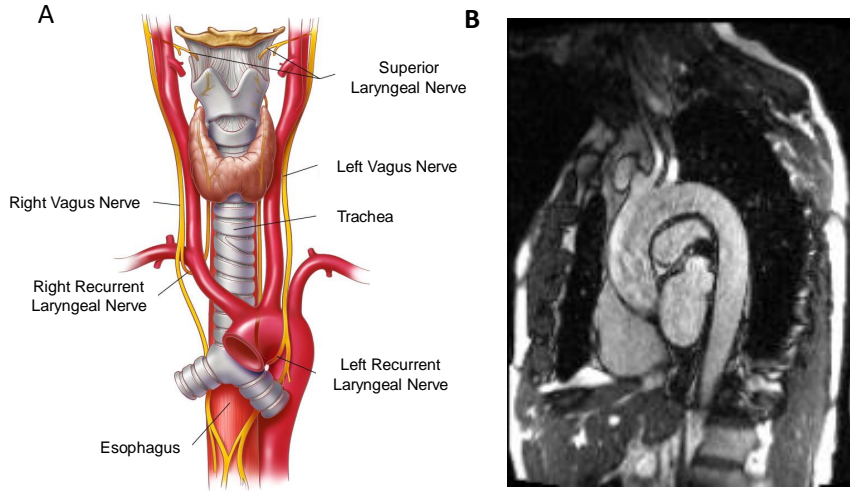


Figure 1: A) Anatomy of the RLN. B) A Sagittal view of the human aorta.

the point of interest selected for aortic diameter measurement for all patients was as close to the brachiocephalic root as possible. Using the plane (ϕ) orientation, an image stack was rotated in 3D space such that aorta cross section at the point of interest became parallel to one of the Cartesian planes (e.g., YZ) (Figure 2B and 2C). The 3D rotation matrix was computed from the multiplication of consecutive rotation matrices.

After rotating the image in 3D, a 2D image segmentation was performed on the cross-section of interest. A 2D segmentation active contours algorithm was utilized [22] to segment the 2D aortic cross-section (Figure 3A) after which a least square ellipse was fitted to the segmented area (Figure 3B). For each subject, the position of the fitted ellipses center and the major and minor axes of the ellipse were recorded over one heart cycle and used in the compliance calculation (Figure 3C). Caudal-cephalic motion of the aorta was also recorded by quantifying the superior-inferior displacement of the center of the ellipse. This was done in order to investigate whether supraphysiological stretch of the left RLN is related to excessive inferior-superior aortic motion.

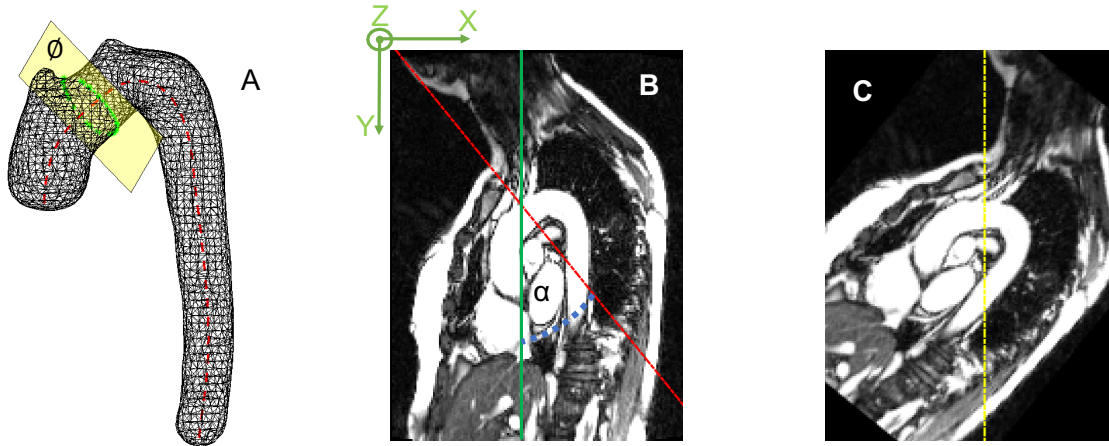


Figure 2: A) 3D reconstructed aorta with the computed centerline and a schematic view of the cutting plane (ϕ). B: The dashed red line is the result of the intersection between one slice of the image stack and the plane (ϕ) to calculate the first angle of rotation. C) The rotated image after the first rotation in XY plane on one sagittal slice.

2.2.4 Statistical Analysis

All participants were categorized into three age groups: Young Group: age less than or equal to 40 years, Middle Age Group: older than 40 years but less than or equal to 60 years, and older age group: over 60 years of age. Gender, age, and group (iUVP, control) were used as the independent variables in our statistical approach, with both main effects and interaction included in the analysis. All image measures were obtained blinded to the condition of the participant being evaluated. Participant group assignment was not revealed for data analysis until all study measures were completed. SPSS (IBM Corp. Released 2013. IBM SPSS Statistics for Windows, Version 24.0. Armonk, NY: IBM Corp.) was employed to perform three-way factorial ANOVA tests to analyze the differences among group means and Tukeys procedure to examine pairwise differences among the three age groups. G*Power [35] was used to perform power analysis and calculate sample size. Values reported are mean \pm standard error of mean unless otherwise stated, and a p-value of <0.05 was considered significant.

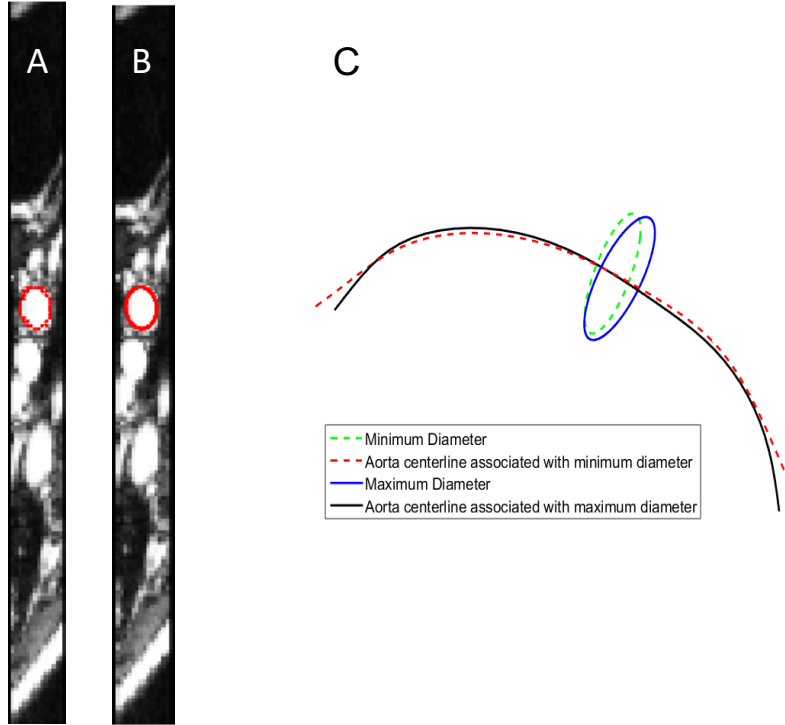


Figure 3: A: An aorta segmented area on a plane normal to centerline close to brachiocephalic root B: The least square ellipse fit to the segmented area C: The aortic centerline and selected cross section close to brachiocephalic branch for maximum and minimum aortic diameter

2.3 Results

For each subject, aortic diameter (Figure 4) was measured at all-time points, and diameter change was calculated respectively.

Figure 5 shows the pulse pressure for both study groups. We found strong evidence to show that age ($p=0.01$) and a three-way interaction of all independent variables ($p=0.04$) have a significant effect on pulse pressure. Post hoc analysis showed that the mean pulse pressure for the young age group was significantly lower than that for the middle and old age group ($p=0.046$ and $p=0.008$, respectively), however, the pulse pressure for those of middle age and old age were not significantly different ($p=0.156$).

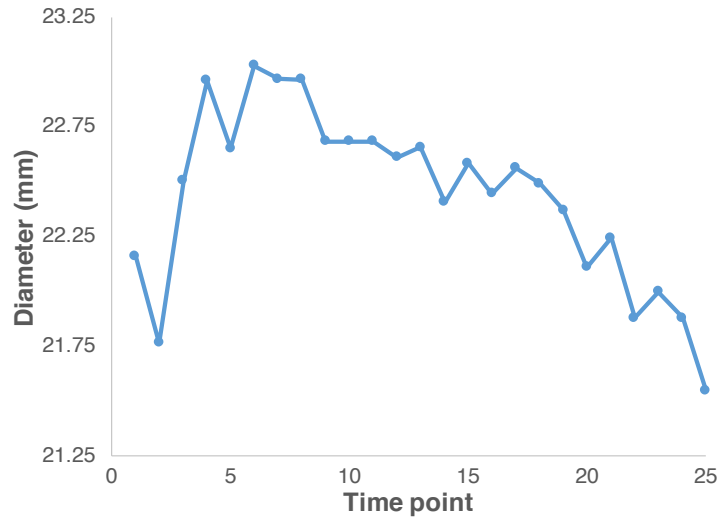


Figure 4: Diameter of a brachiocephalic segment of the aorta for a healthy female, 53 yrs. old

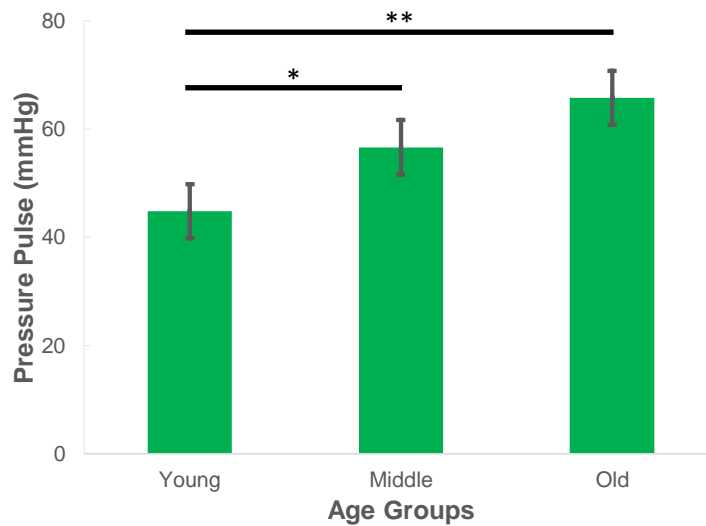


Figure 5: Pressure pulse for all age groups * : post hoc p-value for young and middle age group is 0.046 , **: post hoc p-value for young and old age group is 0.008

Diameter change was defined as the difference between the maximum and minimum diameter of the brachiocephalic segment of the aorta over a cardiac cycle. Aortic diameter change was significantly higher in iUVP patients compared to the control group ($p=0.04$) (Figure 6).

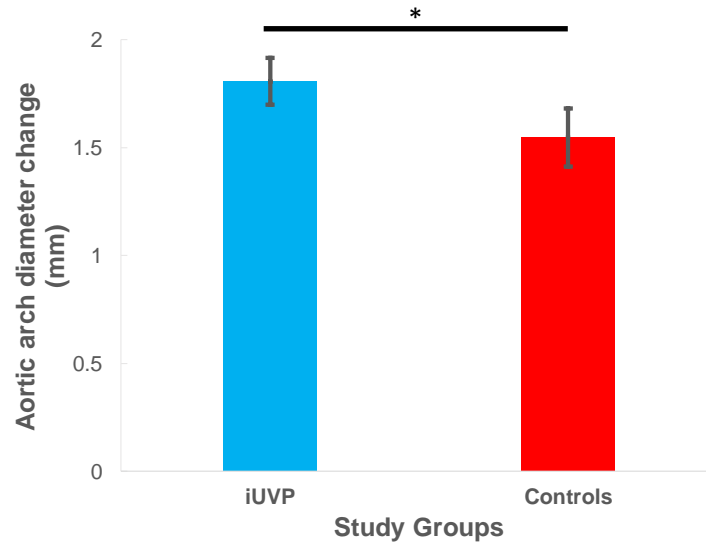


Figure 6: Aortic arch diameter change in healthy people is significantly smaller than iUVP patients ($p=0.04$)

Compliance measures were compared between the idiopathic iUVP and control groups by age (Figure 7). As reported in prior literature, our data confirms that compliance decreases with age for both iUVP and control subjects ($p<0.001$). The mean compliance of the iUVP group was shown to be significantly higher than the control group within the same age group ($p=0.002$). A Tukey's procedure showed compliance among all age group are significantly different as well ($p<0.005$). A post hoc power analysis showed that the group differences in aorta compliance achieved a power level of 99% using an alpha level of 0.05 with a total of 20 observations. However, in order to more thoroughly explore any three-way interactions (disease, age, gender) with the same level of statistical power, a sample size of 150 subjects would be necessary. Recruiting this number of patients was not feasible given the research design and overarching goals of the current study.

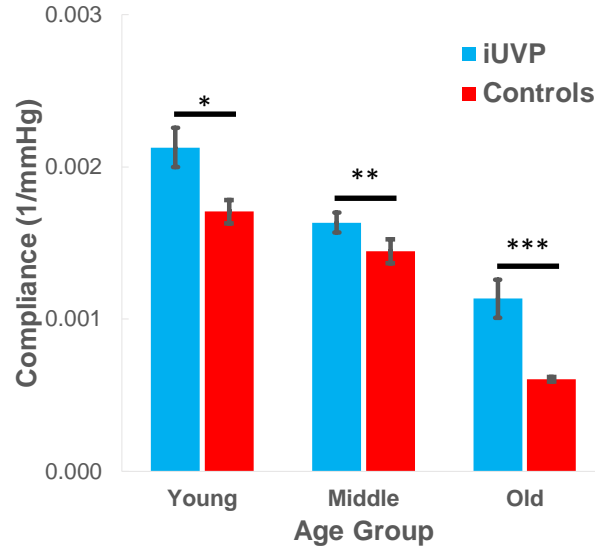


Figure 7: Mean compliance as a function of age and disease. Post hoc p-value between all the age groups are smaller than 0.005

2.4 Discussion

The purpose of this study was to investigate age-related changes in aortic arch compliance as a potential factor in the onset of left-sided idiopathic UVP. Support was found for the hypothesis that aortic arch compliance is greater in those with left-sided iUVP compared to age- and gender-matched controls. More specifically, our findings demonstrated that participants in the idiopathic UVP group exhibited increased aortic compliance at the brachiocephalic artery compared to those in the control group. In general, the findings of this study predict that a one mmHg increase in pressure in iUVP patients will cause a greater change in aortic arch diameter than occurs in age- and gender-matched individuals without iUVP.

Various studies on nerve injury have shown that supraphysiological nerve compression could occur because of the complex and different etiologies, for example when a nerve travels through narrow anatomic openings causing edema, ischemia, and fibrosis [74]. These

findings suggest that a higher load or stretch exerted at this section of the left RLN might result in chronic nerve stretch and/or compression in the context of a hypercompliant aorta that may result in neurapraxia [41]. This condition may result from decreased blood flow within the peripheral nerve due to obstruction of the epineurium blood vessels that it carries along the course of the nerve. An additional source of peripheral nerve vascular impairment occurs in response to compression trauma due to a change in the permeability of the endoneurium microvessels [65]. Also because of the hearts downward motion and aortic pulse during each heart cycle [15], the left RLN experiences a simultaneous combination of stretch and compression. Thus, increased compliance in the context of the complex forces to which the left RLN is exposed could potentially stretch and compress the RLN beyond a physiological level. Prior studies addressing the effect of strain on the peripheral sciatic nerve in the rabbit showed decreases in blood flow by 70-78% during application of strains from 8-16%. Peripheral nerve traction was also shown to reduce the peak velocity significantly at a strain of 16%. Substantial reduction in peak velocity could be a sign of damage to both axons and the myelin sheath [31, 121, 119].

The current study had several limitations that need to be considered in future work. One consideration was the reliance on brachial artery pressure pulse measures to infer blood pressure in the aorta. Avolio [10] showed that pressure obtained from the arm cuff is higher than pressure values in the aorta due to pulse pressure amplification effects. McEniery [71] performed a comprehensive study on more than 5000 subjects to express pulse pressure amplification values according to age. These findings were used to determine how pulse pressure values for the current studys population would differ when adjusted using McEnierys findings. Although adjusted pulse pressures resulted in smaller values for compliance in both the iUVP and control groups, the aortic arch compliance differences between participant groups remained statistically significant ($P=0.045$).

2.5 Conclusion

The current study's findings raise several important questions surrounding the potential role of the compliance of the aortic arch in the onset of left-sided iUVP. Creation of a computational model may be able to systematically test how changes in RLN stress and strain result from changes in aortic arch compliance across age groupings, thus elucidating salient features likely to affect nerve function. Prior work offered preliminary evidence that the aorta could impose higher stress and strain forces on the RLN as a factor in the onset of UVP [122]. Additional consideration is also needed regarding other structures that may similarly impact the left RLN in the context of a hypercompliant aorta such as the pulmonary artery and ligamentum arteriosum. Of great interest will be associated systematic testing of aortic arch displacement and compliance on left RLN function. For example, an ex-vivo model would enable investigation of changes in RLN compound action potentials associated with changes in RLN stretch as imposed by changes in aortic compliance.

In summary, the findings of this study supported the hypothesis that changes in aortic compliance may be a factor in the onset of left-sided idiopathic iUVP. Significantly greater aortic compliance was demonstrated in participants in the iUVP group compared to age- and gender-matched controls. Future work should further explore how left RLN function itself is correlated with its biomechanical environment.

3.0 Specific Aim 2 Determination of the Aortic Arch Mechanical Properties for iUVP Patients and Controls Using *in vivo* Data

In this aim, I studied the mechanical properties of the aortic arch in both iUVP and age-gender matched controls. Variations in the compliance might stem from differences in the biomechanical properties of the individuals in the study group (i.e., iUVP and controls). An inverse finite element approach was utilized to characterize the mechanical properties of the arch using an hyperelastic anisotropic material model.

3.1 Introduction

In chapter two, it was shown that the arch compliance is significantly larger in the iUVP patients compared to the controls. Given compliance of the aortic arch is mainly controlled by its biomechanical properties, characterization of the aortic wall would provide us with invaluable information to better investigate the relationship between cardiovascular system and the RLN damage.

The aortic wall has a fairly complicated structure. It consists of three distinct layers, intima, media, and adventitia. In the young and healthy individuals, the innermost (i.e., intima) and the outermost (i.e., adventitia) layers minimally contribute to the aortic wall mechanical properties. A closer look at the aortic wall tissue reveals that the media layer is divided into many transversely isotropic fiber-reinforced segments. These units are made of interconnected elastin and collagen fibrils, elastic laminae, and smooth muscle cells and dictate the load-bearing and elastic behavior of the tissue [89, 49, 79, 118]. Several studies have shown that an anisotropic hyperelastic constitutive model in which stress-strain relationship drives from a strain energy density function, can adequately describe soft tissue behavior. Gasser et al. have proposed a hyperelastic constitutive model that includes the effect of the collagen fiber orientation dispersion [37]. The proposed model is a generalization of the fiber-reinforced constitutive model introduced by Holzapfel et al. [49, 50]. The biaxial tensile

testing methods have been used extensively to characterize the biomechanical properties of the soft tissue [127, 45, 39, 40, 100]. The *ex vivo* tests are essential to develop and examine constitutive models; however, natural biological environment (i.e., *in vivo* conditions) including hormonal stimuli and perivascular tethering are absent in an *ex vivo* testing condition [70]. A few studies have characterized mechanical properties of the arterial wall using *in vivo* data. Masson et al. used an inverse finite element approach to characterize the mechanical properties of the Carotid artery using human clinical data. Pressure, wall thickness, and geometry of the carotid artery were collected for each patient and were imposed on the model. The optimization problem was then solved using a nonlinear least-squares minimization algorithm to fit for the material constants and other unknowns [70, 69].

In this study, we determined the *in vivo* mechanical properties of the aortic arch using patient-specific data. We utilized an inverse finite element approach in a metaheuristic optimization framework and developed patient-specific models to evaluate the mechanical properties of the human aortic arch in iUVP patients and age-gender matched controls. Gated MRI images were used to create patient-specific geometry and calculate displacement boundary conditions. Given the well-established history of the significant connection between UVP and some cardiothoracic diseases, We believe that the results of this study notably promotes our understanding of the potential RLN damages related to the biomechanical environment of the nerve. In addition, our proposed computational framework could be used as an efficient and noninvasive approach to evaluate the mechanical properties of the aortic arch as they relate to the onset and progression of several other medical conditions.

3.2 Methods

3.2.1 Study Population & Imaging Protocol

Study population and Imaging protocol were defined in sections 2.2.1 and 2.2.2. We used 3D image stacks collected from twenty subjects, ten iUVP patients and ten age-gender matched controls.

3.2.2 Image Processing and Geometry Creation

Gated MR images were acquired at 25-time points over one cardiac cycle. This enabled us to determine aortic arch diameter change for all the subjects at the location of the brachiocephalic artery which is known to be the junction point of the left recurrent laryngeal nerve and aortic arch. A custom MATLAB code was developed based on the active counter method to create a 3D geometry of the aortic arch at the minimum diastolic state. During image segmentation and reconstruction of the arch geometry, stiffness of the initial counter was adjusted such that all the arteries were excluded from the geometry [11, 22]. In the next step, the arch centerline was computed [8, 9], and the reconstructed geometry was then cut orthogonal to the centerline at several spots including the location of the brachiocephalic artery (Figure 8A). Subsequently, a 3D loft was performed using a MATLAB costume code to create the computational model of the aortic arch (Figure 8B). The entire process of the geometry creation (i.e., segmentation, detection and removal of the arteries, slicing of the geometry, and loft) was automated to eliminate user inter and intra-variability.

3.2.3 Displacement Field Calculation

A digital volume correlation (DVC) algorithm was used to compute the displacement field between minimum systolic and maximum diastolic time points for each subject. A non-rigid image registration technique based on Thirion's demon algorithm was employed to determine the displacement field. This algorithm utilized the concept of diffusing models (i.e. deformable grid), which is a robust and computationally efficient image registration approach [84, 116]. The details of the displacement field computation could be found in another published work from our group [14]. Upon completion of the displacement calculation, a 3D Gaussian low-pass filter was applied to the displacement field to minimize the effect of the noise and estimation error [25].

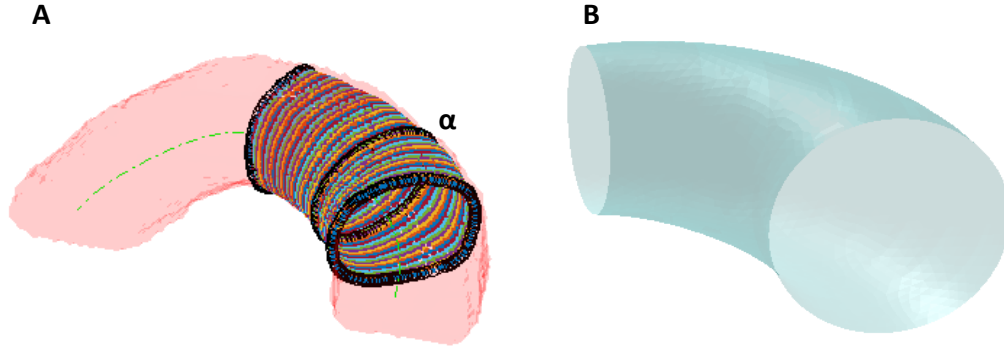


Figure 8: A) The reconstructed geometry was cut normal to the aorta centerline, and then an ellipse was fitted to each cross-section. (α) shows the location of the brachycephalic artery B) The geometrical model was created by performing a 3D loft using the elliptical cross-sections and centerline.

3.2.4 Finite Element Model and Optimization

The collagen fiber reinforced structure of the aortic arch could be properly characterized by an incompressible, anisotropic, hyperelastic constitutive model. We adopted a material model which was primarily proposed by Holzapfel et al. [37, 49]. The strain energy function U can be expressed as:

$$U = C_{10}(\bar{I}_1 - 3) + \frac{1}{D} \left(\frac{(J^{el})^2 - 1}{2} - \ln J^{el} \right) + \frac{k_1}{2k_2} \sum_{\alpha=1}^N \exp(k_2(\bar{E}_\alpha)^2) - 1 \quad (3.1)$$

where,

$$\bar{E}_\alpha = \kappa(\bar{I}_1 - 3) + (1 - 3\kappa)(\bar{I}_{4(aa)} - 1) \quad (3.2)$$

$$\bar{I}_{4(aa)} = A_a \cdot \bar{C} \cdot A_a \quad (3.3)$$

$$\kappa = \frac{1}{4} \int_0^\pi \rho(\theta) \sin^3 \theta d\theta \quad (3.4)$$

In this model, the aortic tissue was assumed to be composed of a matrix material with different families of embedded fibers. Each family fiber has a preferred direction which was introduced in the model by γ . \bar{I}_1 is the first deviatoric invariant, $\bar{I}_{4(aa)}$ is the pseudo-invariants of distortional part of the right Cauchy-Green strain and the set of the unit vectors that characterize the reference configuration of each family fiber direction. C_{10} is matrix stiffness, D determine the incompressibility, K_1 is the fiber stiffness, K_2 is dimensionless parameter that expresses the linear behavior of material after all the collagen fibers are fully recruited. κ describes the level of dispersion in the fiber directions and it varies between 0 for perfect alignment and $\frac{1}{3}$ for random distribution. It is also assumed that all families of fibers have the same mechanical properties and the same dispersion. The Holzapfel material model requires a local coordinate system and preferred orientation for each element. Haskett et al. [45] used small-angle light scattering (SALS) technique to study collagen fiber orientation as a function of location and age in the human aorta. Collagen fiber orientation data was borrowed from the prior study, and we hypothesized that it doesn't vary across the healthy and iUVP patients.

Finite-strain shell elements (S3R) were used to mesh the geometry in ABAQUS. Circumferential (hoop) stress at the location of the brachiocephalic artery for different element size was studied to achieve a mesh independent solution (Figure 9 A&B).

A two steps finite element model was designed and solved in an iterative fashion to fit for the unknown mechanical and geometrical constants using ABAQUS standard solver. A MATLAB code was developed to segment the MRI images, write a simulation input file and implement a global optimization scheme (i.e. particle swarm). In the first step of the simulation, arch geometry at the zero-pressure configuration was inflated to the minimum

systolic pressure. All the nodes located at both ends of the geometry were restricted to move in radial direction. In the second step, inflation continued to the maximum diastolic pressure level with the displacement boundary conditions applied at both ends. To create the zero-pressure configuration, the segmented arch geometry at the minimum diameter state was shrunk radially. As zero-pressure configuration is unknown, the percentage shrinkage was parametrized by defining an independent variable (δ) which was considered as an open parameter in the optimization.

Additionally, MRI imaging did not yield information about the aortic arch wall thick-

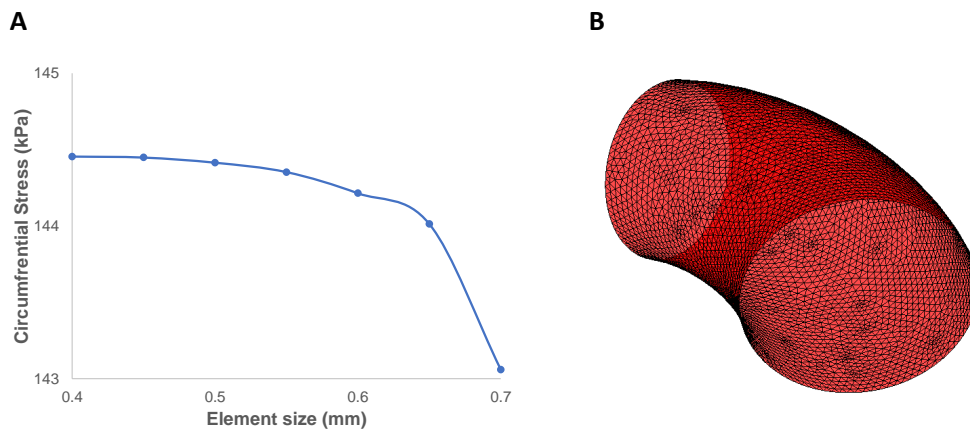


Figure 9: A) Mesh independency study for the arch model B) S3R elements were used to mesh the aortic arch.

ness. Different studies have shown that aortic wall thickness changes with age, race [47, 68]. Li et al. utilized MRI images and assessed aortic arch wall thickness for different age group [35]. Fitting a 1st order polynomial to the thickness data from the previous study enabled us to formulate the wall thickness as a function of age (Figure 10). As differences in the aortic arch compliance could originate from the aortic wall thickness, we used the lower bound of the wall thickness and recalculated the material parameters [60]. Proper choice of the objective function, optimization method, and constraints were crucial to achieve a valid set of the

material and geometrical constants for the aortic arch. The objective function was designed to minimize the difference between the computational arch diameter (d_{comp}) resulted from solving the simulation problem and the experimental diameter of the arch (d_{exp}) calculated from MRI images [13]. As the material behavior was described using a nonlinear constitutive model, diameter comparison was performed at several time points between the minimum and maximum arch diameter:

$$f = \frac{1}{n} \sum_{i=1}^n \frac{|d_i^{exp} - d_i^{comp}|}{d_i^{exp}} \quad (3.5)$$

As solving an optimization problem by using deterministic methods in a 4D space was computationally expensive, we utilized a metaheuristic global optimization paradigm, which is called particle swarm optimization (PSO) method [102]. PSO shares many similarities with evolutionary computation techniques such as genetic algorithms. This method starts by creating an array of the random initial guesses (i.e. particles) with assigned initial velocities. During each iteration, it evaluates the objective function for all the particle to determine the lowest function value then PSO updates velocities and location for all the particle-based on the findings from the previous iteration. This process continues until the algorithm reaches the stopping criterion . The initial guesses (C_{10}, K_1, K_2 and δ) were needed for each iteration. Also, we defined boundaries for the parameters based on the physiological data [45, 70, 69]. A design of experiments (DOE) study was performed to evaluate objective function values at different combination of the unknown parameters. The results of the DOE study were later used to create a set of educated initial guesses that resulted in faster convergence. We utilized parallel processing to solve the simulations; thus, a scaling study was performed to calculate the optimum number of the CPUs needed for each simulation. As calling more CPU cores would increase the communication time between the CPU workers, there is an optimum number of the cores for each simulation problem based on the problem size. Our study showed that using six CPUs can significantly decrease the run time (figure 11).

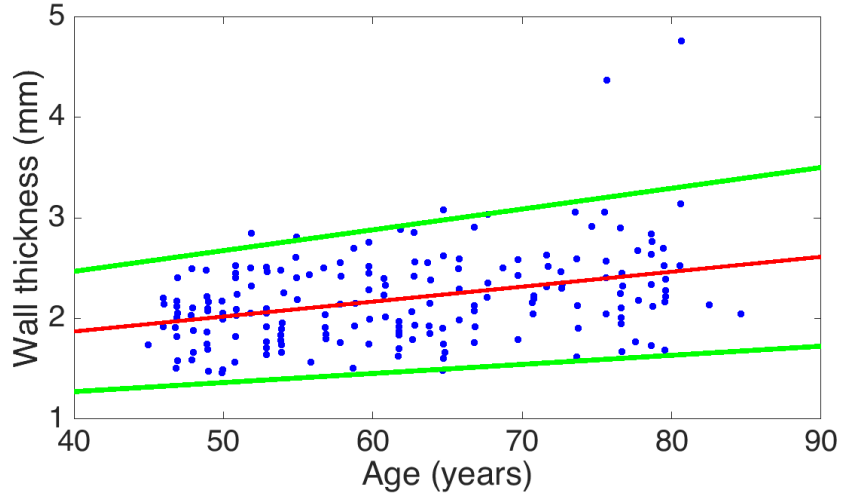


Figure 10: Wall thickness was defined as a function of age.

3.2.5 Statistical Analysis

As it was described before, the study group for this aim was similar to the study group in the aim 1; thus, we used three-way factorial ANOVA test to analyze the differences among group means. Gender, age, and group (iUVP, control) were used as the independent variables in our statistical approach, with both main effects and interaction included in the analysis. The pairwise comparisons were performed using Tukey test and p-value of <0.05 was considered significant.

3.3 Results

The DOE study and the optimization were implemented for all 20 patients. Our results showed several significant differences between the study groups. As depicted in Figure 12, age was a significant effect for matrix stiffness (C_{10}) of the aortic arch in both iUVP and

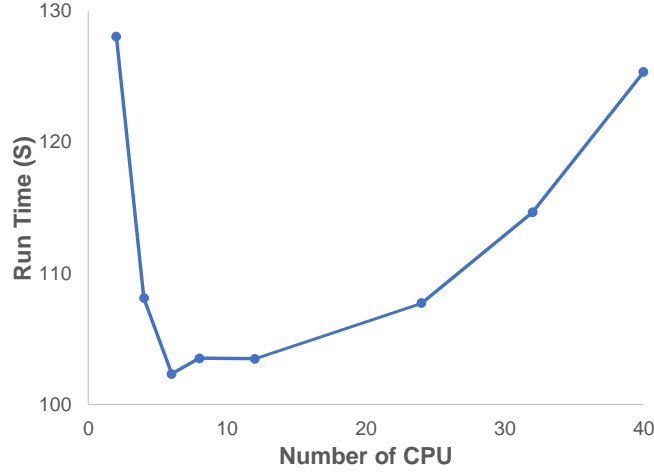


Figure 11: Utilization of the 6 cores resulted in the optimum computational cost

healthy subjects. Matrix stiffness was significantly smaller in young health group compared to middle age (p-value = 0.0024) and old group (p-value <0.0001). Stiffness of the matrix was smaller in healthy middle-age subjects versus old age group (p-value= 0.0047). In addition, C_{10} was significantly smaller in the young iUVP group compared to the diseased middle age (p-value= 0.0002) and old age group (p-value= 0.0004). Our study also showed that the matrix stiffness in old iUVP group is significantly smaller than the healthy old subjects (p-value = 0.035). Collagen fiber stiffness (K_1) was also statistically different across the study groups. As illustrated in Figure 13., age group and disease were both main effects for the fiber stiffness in both healthy and iUVP subjects. We showed that K_1 is significantly smaller in the healthy young group compared to the healthy old group (p-value=0.0002). Furthermore, in iUVP group, fiber stiffness was smaller in the young group compared to the middle age (p-value=0.0053) and old subjects (p-value=0.0002). It was also shown that fiber stiffness is smaller in the healthy middle age group than the healthy old group (p-value=0.0008). Our study showed that K_1 is significantly smaller in iUVP old subjects compared to the healthy

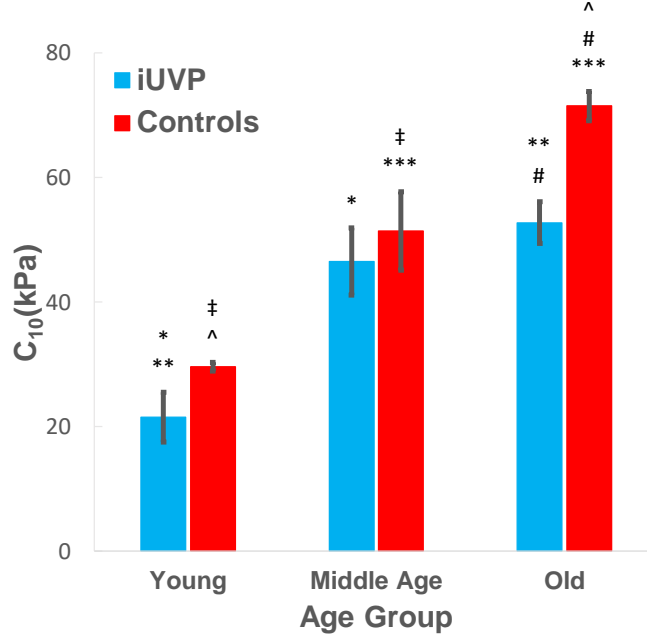


Figure 12: Age group and disease were significant effects for the stiffness of the matrix. C_{10} was smaller in the old iUVP group compared to the same age group of the controls (p-value = 0.035)

old group (p-value=0.047). As shown in figure 14, A significant effect was identified for the age group with the fiber stiffness (K_2) being larger in both healthy and iUVP old age groups than the young and middle age groups (all p-values < 0.0001). Moreover, the iUVP was a significant effect for K_2 as it was higher in the healthy group compared to the iUVP group iUVP across the old age subjects (p-value=0.032). Figure 15 showed that the age group was a significant effect for the percentage shrinkage as it was smaller in the healthy old group than the healthy young (p-value=0.0014) and middle age groups (p-value=0.0332).

In addition, A significant main effect was identified for the age group with the percentage shrinkage being larger in old iUVP group than the young iUVP group (p-values=0.0041). Finally, we considered the thickness values based on the lower bound of the 95% confidence level to investigate the relationship between the calculated material parameters and thickness. Our study also showed that the thickness is not a significant main effect for

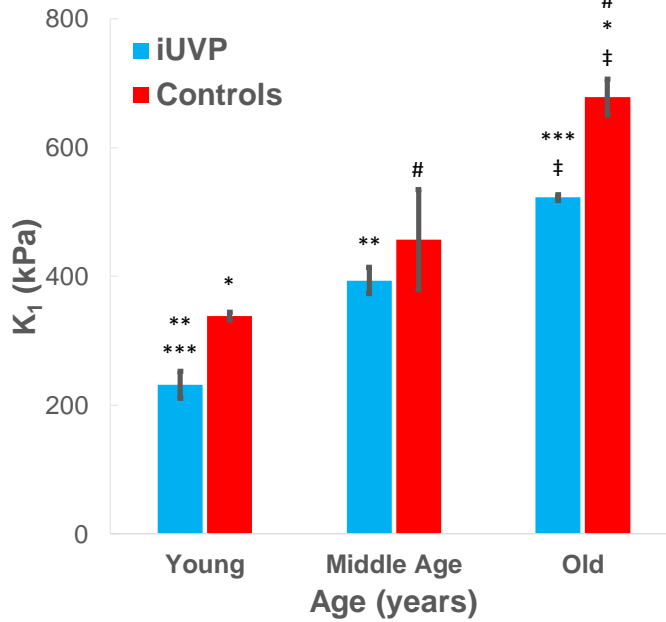


Figure 13: Fiber stiffness (K_1) increased significantly with age in iUVP subjects and controls. It was also greater in the control group than the iUVP group within the old age group (p-value=0.047)

the observed differences in the matrix stiffness within the old age group (p-value =0.13). However, the statistical analysis showed that all other material parameters and percentage shrinkage increased significantly with decreased thickness.

3.4 Discussion

We have presented a computational framework to characterize mechanical properties of the aortic arch using *in vivo* information in iUVP patients and age-gender matched controls. Our study showed several significant differences in the mechanical properties of the aortic wall across the various study groups by utilized an inverse finite element approach. Experimental methods (i.e., *ex vivo* experiments) are the first step toward soft tissue mechanical

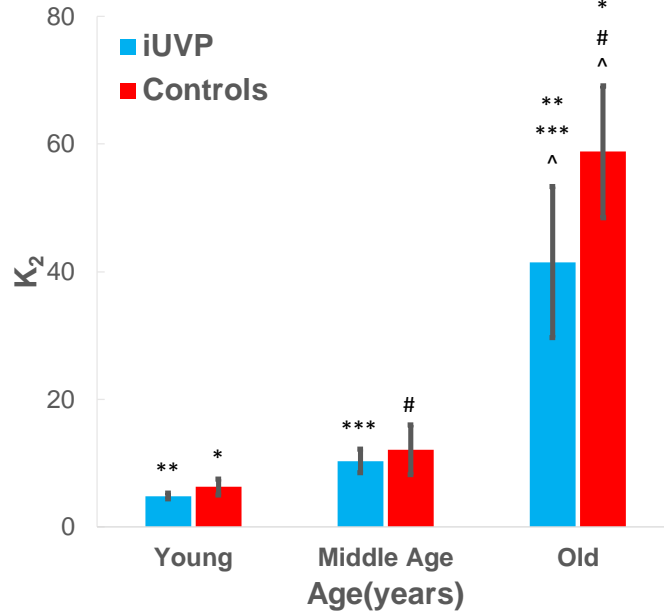


Figure 14: Age group and disease were significant effects for the fiber stiffness parameter. It was significantly smaller in the old iUVP group than the old control subjects (p-value=0.032).

properties characterization. Several studies have used the biaxial tensile test to study the biomechanical behavior of the aortic wall. Haskett et al. studied microstructural and biomechanical alteration of the human aorta as a function of age and location [45].

In addition, Vande Geest et al. experimentally investigated biomechanical behavior of the human abdominal aorta in healthy and aneurysmal tissue using Fung constitutive model [40, 39]. The prior work provided us with invaluable information that confirms the validity of the proposed material model, microstructural information, and tissue behavior in the *ex vivo* setup. As the determination of the nonlinear and anisotropic aortic wall properties by inverse methods tends to be an ill-posed problem, navigating the optimization algorithm by defining the physiological bounds or replacing the unknown values with the experimental data would help regulate and stabilize the numerical approaches. That being said, in our study, we borrowed fiber splay data, physiological bounds for the material properties and

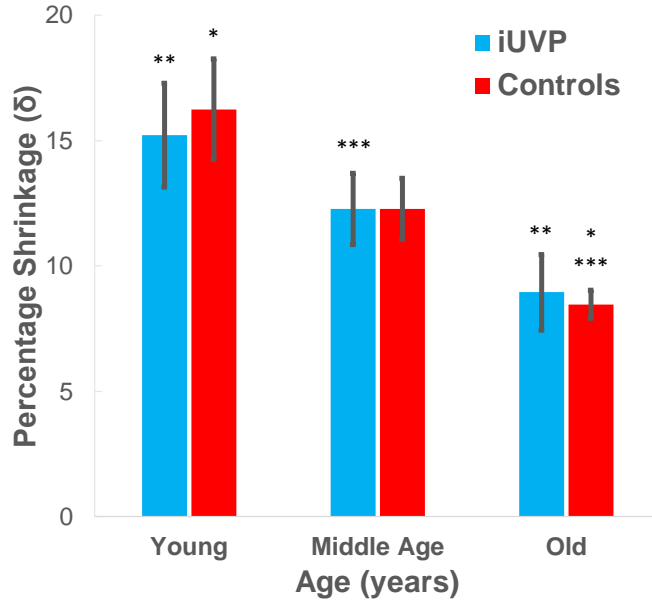


Figure 15: Age group was the only significant effect for the percentage shrinkage parameter.

wall thickness from other work to more focus on the anisotropic material properties of the aortic wall as it relates to the hypercompliant behavior of the arch in iUVP patients.

In the finite element modeling, the validity of the boundary conditions vastly affect the results. Wittek et al. utilized a three-dimensional ultrasound speckle tracking method and estimated wall motion of the human ascending and abdominal aorta [125]. A few limitations, such as the low resolution of the images or depth-limitation inherent in ultrasound imaging affected the results adversely. In our proposed method for displacement field calculation, we can use any medical images (e.g., CT, MRI) with higher resolution. Additionally, depth limitation would not be a restriction in CT or MRI imaging.

Several experimental and computational studies have demonstrated that the biomechanical behavior of the soft tissues in a function of age in human. Haskett et al. showed that matrix stiffness, fiber stiffness and fiber parameter increase with age [21]. Increased C_{10} and K_1 directly contribute to the increased stiffness of the aortic wall. Additionally, Vande Geest et al. showed that the peak of the longitudinal and circumferential stretch of the human

abdominal aorta decreases with age [39]. Our finding was consistent with prior studies as we showed that C_{10} , K_1 , and K_2 increased with age regardless of disease.

There are a few studies that have used inverse approaches to characterize the mechanical properties of the arterial system. Masson et al. used *in vivo* data in an inverse finite element configuration and determined that mechanical properties of the carotid artery [70]. The authors successfully modeled residual stress, axial pre-stretch, smooth muscle cells contraction, and hyperelastic behavior of the arterial wall. A cylinder was considered as the base geometry for the carotid artery which enabled the researchers to parameterize the stress-free state and the opening angle. The diameter of the artery and blood pressure were collected for each patient. The objective function was defined to compare computed and measured intraluminal pressure, and it was minimized by applying a local optimization technique. In another attempt, Wittek et al. used the 4D ultrasound imaging and determined the anisotropic hyperelastic properties of the normal and diseased (i.e., aneurysm) abdominal aortic wall [124]. This study provided an efficient computational approach for the inverse finite element setup; however, small sample size, constant thickness, and the treatment of the zero-load configuration were the main limitations of this study. In our study, we parametrized the zero-pressure configuration by introducing the percentage shrinkage factor (δ) as an open parameter in the optimization. Moreover, thickness data was defined as a function of age. Nevertheless, including patient specific thickness measurements in the model in the best approach as it would eliminate the dependency of the results to the thickness variation.

Given the complexity of the inverse finite element problems, some investigators have used machine learning (ML) techniques to improve the computational methods in the biomechanics. Liu et al. developed an ML-based approach to estimate the *in vivo* constitutive parameters of the aortic wall [63]. The ML-models would significantly improve the quality and speed of the material characterization; however, the inverse finite element approach builds the bases for the statistical model and training data set required in the ML-models. The architecture of the aortic arch primarily defines the mechanical properties of the tissue. The major constituents of the aortic arch ECM are fibrous proteins(i.e., collagen, elastin, fibronectins, and laminins) and proteoglycans (i.e., hyaluronic acid, heparan sulfate, and keratin sulfate). The fibrous proteins mainly contribute to mechanical structure and rate of

remodeling and degradation of the ECM [86]. Collagen is the primary structural element of the ECM provides the structural integrity and tensile strength of tissues, regulates cell adhesion [95]. Collagen related diseases mostly originate from genetic defects or nutritional deficiencies that affect the processes involved in normal collagen production. In contrast, elastin provides the elastic and recoil properties of tissues that undergo repetitive stretching. Several studies have shown that connective tissue disorders such as Systemic lupus erythematosus (SLE), systemic sclerosis (SSc) could affect the various organs in the body by causing structural alterations [38]. Interestingly, a study by Imauchi et al. reported a connection between SLE and paralysis of the left vocal cord [52]. Furthermore, other connective tissue disorders such as Marfans syndrome can adversely affect the integrity of the cardiovascular tissue structure in different levels [72]. Also, several studies have shown that type I collagen disorders such as osteogenesis imperfecta are linked to cardiovascular diseases [126]. We showed that several constitutive parameters in the iUVP patients are smaller compared to the normal controls. In the absence of the proper structural stiffness in the iUVP patients, a chronic supraphysiological load might be exerted on the RLN over a long period. Several studies have shown that chronic compression or stretch might cause irreversible damage to the RLN [66, 98, 26].

There are several limitations associated with this study. Axial pre-stretch and circumferential residual stress were not included in the computational model. Also, blood pressure measurements were collected from the left brachial artery, not the aortic arch. However, our previous study showed similar differences in the aortic arch compliance using the corrected pressure pulse [13]. We assumed that there is not an association between the collagen fiber splay, preferred orientation, and the aortic wall thickness. However, another experimental study is essential to investigate any differences in the morphological properties across the study groups.

3.5 Conclusion

In conclusion, we showed that the mechanical properties of the aortic arch are different between iUVP patients and age-gender match controls. We also presented an efficient computational framework to determine the mechanical properties of the aortic wall using *in vivo* data. The combination of the global optimization approach and the extensive DOE study enabled us to improve the confidence level of capturing the global minimum of the objective function. The future direction for this study could include residual stress and smooth muscle cells contraction to better describe the biomechanical behavior of the aortic arch. We believe that the results of this study would significantly promote our understanding of the cardiovascular system interaction with the recurrent laryngeal nerve. The proposed methods in this study could be later used to construct a computational framework to fully study RLN behavior in response to variation in the biomechanical properties of the aortic arch.

4.0 Specific Aim 3 Extracellular matrix deformations of the porcine recurrent laryngeal nerve in response to compression

In this aim, I focused on studying the biomechanical response of the RLN under compression. As the suprphysiological level of compression leads to different types of nerve injury, the results of this study would pave our path to understand how RLN injury may occur as a result of the nerve compression by a hypercompliant aortic arch or other pathophysiological conditions such as edema.

4.1 Introduction

As discussed in chapter two, the RLN damage due to the unfavorable changes in the nerve biomechanical environment could be a potential cause for the onset of the left-sided UVP. A higher level of mechanical loading, including compression and stretch, could adversely influence the functionality of the RLN and causes reversible or permanent injuries. The severity of the nerve damage depends on both the intensity and duration of the mechanical insult. Nerve injuries are classified into three categories, based on the presence of demyelination and the level of the damage to the nerve connective tissue and axons [3]. Neurapraxia is the mildest type of injury which includes focal demyelination without any damage to connective tissues or axons of the nerve. In axonotmesis or second level of the nerve damage, axonal damage, and focal demyelination occur; however, the integrity of the nerve connective tissue is still maintained. Lastly, nerve injuries that exhibit full transection of the axons and connective tissues are categorized as neurotmesis [74]. In the absence of traumatic injuries, nerve damage due to compression is mostly limited to neurapraxia and axonotmesis; nevertheless, chronic nerve compression may lead to Wallerian degeneration, and consequently, irreversible loss of nerve function [2].

A closer look at the architecture of the peripheral nerve reveals that there are several layers of the connective tissues to protect and isolate the axons against stretch and compression.

The innermost layer is called endoneurium, which encapsulates individual axon. The bundle of the axons is contained in the perineurium layer and form a nerve fascicle. Epineurium is the outermost layer of the peripheral nerve that encloses nerve fascicles and microvasculature [117]. In epineurium, collagen and elastin are mainly oriented longitudinally. In contrast, collagen fibers and fibroblasts are organized in concentric layers in perineurium [113, 111, 21]. Adipose and elastin are also presented in Epineurium [85]. Different components of the RLN extracellular matrix function together and contribute to the mechanical properties of the tissue. For instance, some researchers have suggested that epineural collagen provides mechanical stiffness in stretch [29, 30], while adipose protects the axons against compression [112]. Furthermore, several studies have shown that the composition of the nerve varies along the length of the nerve. Barkmeier et al. performed an extensive quantitative analysis on canine RLN and showed gradual changes in the relative epineural area occurred from proximal (i.e., near to the aortic arch) to the distal (i.e., close to the neck) segment of the RLN [12]. In addition, Williams et al. mechanically evaluated different segments of juvenile and adolescent pig RLN using uni-axial test. They found significant differences in the tangential modulus, strain energy density, and collagen fiber splay between various segments of the RLN [123, 5]. The RLN composition dictates the biomechanical properties and biomechanical response of the nerve under mechanical insult. Sunderland hypothesized that there is a significant connection between the biomechanical environment (i.e., location) and peripheral nerve composition. For example, he showed that the proportion of nerve epineurium is greater, where a higher level of mechanical loading is applied to the nerve (e.g., joints) [113, 111, 114]. Furthermore, Campbell et al. used stereology to study proportion and composition of the pig RLN connective tissue. They showed that juvenile pigs had a higher percentage of collagen in the proximal segment of both sides of the RLN compared to adolescent pigs [21]. Williams et al. also showed that left segments of the pig right RLN have different mechanical properties compared to the left side nerve [123]. Consistent with Sunderlands theory, the above studies suggest that the spatial disparity in the nerve composition occurs to tune the mechanical properties of the tissue and compensate for the differences in the environmental loading conditions. Given the RLN injury may happen because of the supraphysiological level of compression caused by a hypercompliant aortic arch

or a pathophysiological event such as edema, the purpose of this study was to investigate the biomechanical response of the RLN under compression as it relates to the onset of the iUVP. Second-harmonic generation (SHG) imaging was used to capture deformation of the RLN connective tissue at different pressure levels and determine the biomechanical response of the RLN as a function of location and age. Several studies have shown similarities between laryngeal innervation patterns, RLN anatomy, and function in human and porcine [36-38]; therefore, we employed a porcine model to conduct mechanical testing. Finally, a histological study was performed to examine the variation of the RLN collagen fibers orientation under compression.

4.2 Methods

4.2.1 Sample Acquisition and Preparation

The RLN excised bilaterally in 9 piglets (10 to 20-day old weeks old, four males and five females) and eight pigs (3 to 4-month-old, four males and four females) within 2 hrs. postmortem (Figure 16). The samples were stored in physiological saline at 4 C. All the nerve specimen was isolated from the insertion point into the larynx to the vagus nerve. To maintain the orientation of the proximal and distal end of the RLN nerve, a segment of the vagus nerve was excised with the RLN branch. Using micro scissors and dissecting microscope (Olympus-SZX7), adipose, and other connective tissues were removed from the samples. The nerve was divided and cut into distal, proximal, and middle segments. The distal and proximal segments were mechanically tested while the middle section was fixed in 10% formalin as control. The control samples were later used for histological studies to investigate the compression effect on the nerve diameter and collagen fiber orientation. Upon completion of the compression test, all the samples were stored in 10% formalin at 80 mmHg for 24 hrs. to perform the histological studies.

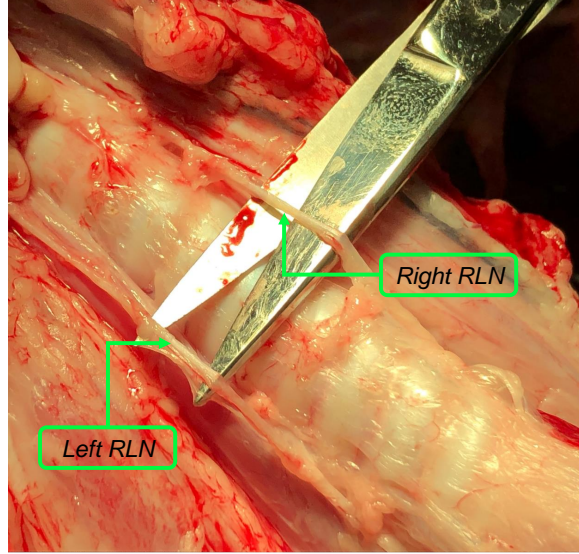


Figure 16: Left and right RLN of an adolescent porcine

4.2.2 Compression Test and Imaging

Biomechanical response of the RLN under hydrostatic compression was studied using a chamber (Figure 17A) which was designed to maintain pressure up to 80 mmHg. A Cartesian coordinate system was defined to determine the various strain components in the samples (Figure 17 B). Both ends of each specimen were glued to a cover-slip such that the sample stays in place during the mechanical testing (Figure 17C). The RLN segment was then placed into the compression chamber, and the lid was secured to maintain the pressure at the various levels. A small hatch was designed on the chamber lid for imaging the specimen during the mechanical testing. A hydrostatic column was used to create the desired pressure in the chamber. The SHG imaging was performed at 0, 40, and 80 mmHg. At each pressure level, a 30-minute wait time was considered to minimize the effect of the creep.

The samples were imaged using an Olympus BX51 upright laser-scanning microscope, shown in Figure 18A, which was coupled to a coherent 120-fs tunable pulsed titanium-

sapphire laser (Chameleon ultraii, Coherent Inc., Santa Clara, CA). The laser was centered at $\lambda = 780$ nm to efficiently visualize collagen via SHG. Digital images were acquired with a plan-apochromat lens with a magnification of 10X, numerical aperture = 0.3, a working distance of 3.8 mm, and a pixel size of 0.96 μ m in the x- and y-direction and three μ m in the z-direction with automatic focusing. The dimension of each 2D image was 1042 \times 1042 pixels, and they were stored as 16 bits per pixel. An example of a mean intensity projection of the RLN is shown in Figure 18B. Due to a loss of signal at increased imaging depth, we excluded data deeper than 250 μ m from the surface of the RLN in our displacement and strain calculations.

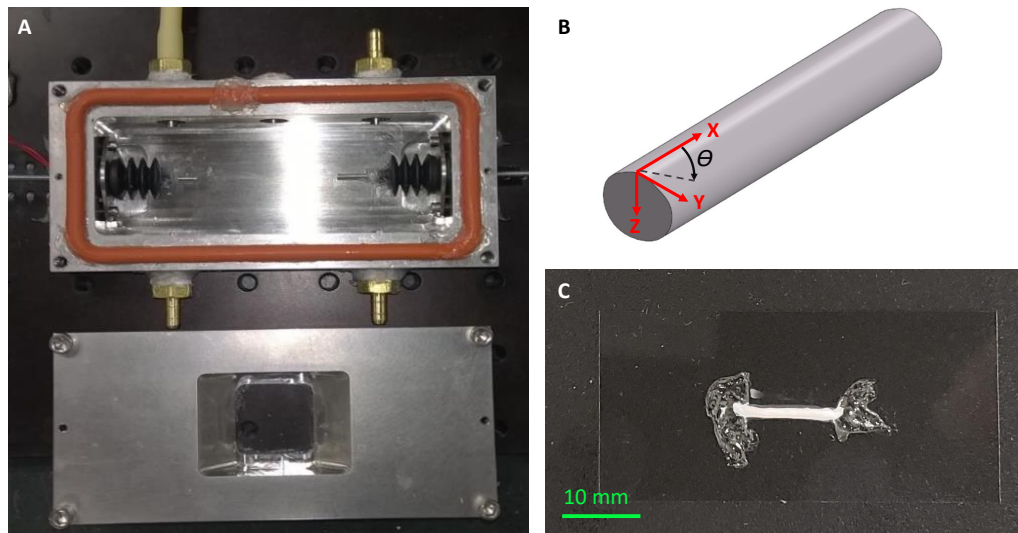


Figure 17: A) compression chamber was designed to maintain hydrostatic pressure up to 80 mmHg. B) A Cartesian coordinate system was defined to investigate specimen strain field. C) The nerve specimen was glued to a coverslip. SHG Imaging was performed at the center point of the sample under compression.

4.2.3 Displacement and Strain Calculation

A DVC algorithm was used to compute the displacement field at increasing pressure for each sample. There are different algorithms [67, 43, 58] that can be used to compute the displacement field at each pressure level. However, we needed a method that accounts for all types of displacement (i.e., translation, rotation, shear, and scale). In this study, we employed a non-rigid image registration technique based on Thirion's demon to calculate the displacement field. This algorithm utilized the concept of diffusing models (i.e., deformable grid), which is a robust and computationally efficient image registration approach [116, 84]. Additional details of the DVC algorithm implementation were included in another published study from our research group [14]. Upon completion of the displacement field calculation, a 3D Gaussian low-pass filter was applied to the displacement field to minimize the effect of the noise and estimation error on the strain calculation [25].

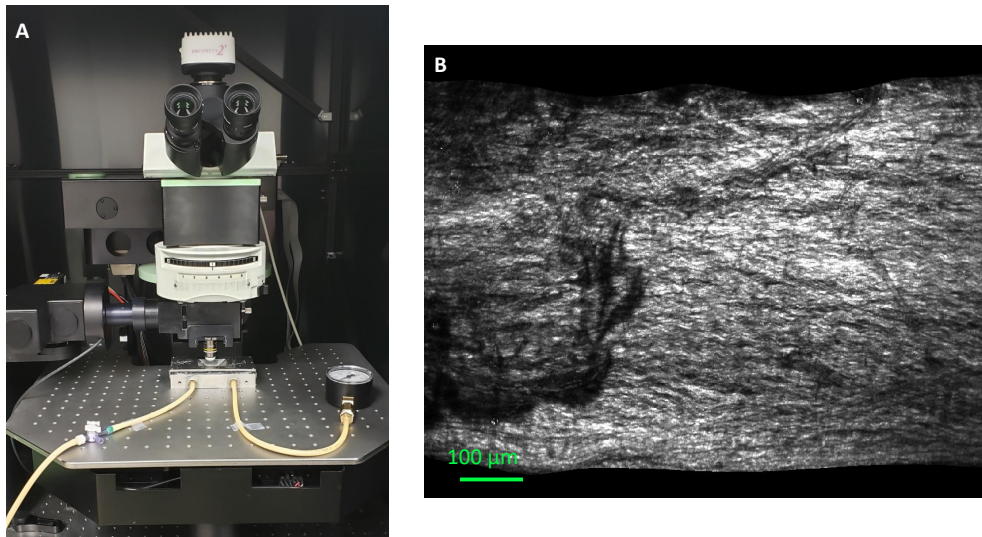


Figure 18: A) Experimental setup under the multiphoton microscope to collect SHG signals. B) Mean intensity projection of a representative left RLN from a piglet at 0 mmHg.

The displacement results were then used to calculate strain, which is the relative displacement between particles in a material body. The Green strain tensor (\mathbf{E}) is defined as:

$$E = \frac{1}{2}(\mathbf{F}^T \mathbf{F} - \mathbf{I}) \quad (4.1)$$

$$F = \frac{\partial \mathbf{u}}{\partial X} + \mathbf{I} \quad (4.2)$$

\mathbf{F} is the deformation gradient tensor, \mathbf{I} is the identity matrix and, the displacement field is denoted as \mathbf{u} . A Cartesian coordinate system was defined as depicted in Figure 2B. The x-axis was set in the axial direction of the nerve specimen, and Z-axis was defined from the nerve top surface inward. The partial derivative of the displacement field and the strain tensor were calculated using a MATLAB code developed by Kroon [55, 4]. Lastly, the minimum detectable difference for the displacement field components was determined to filter noise from the actual displacement field. This was done by imaging one sample twice without making any changes in the imaging setting. As pressure was kept unchanged, displacement gradient should be zero, but due to imaging noise and round off/truncation error, a non-zero displacement field was observed. The average \pm standard deviation of each displacement field component was used to define the noise level. We filtered any strain value resulted from a displacement field with components smaller than the noise level. Noise levels of each displacement component were $u_x = 0.45 \pm 0.11 \mu\text{m}$, $u_y = 0.59 \pm 0.29 \mu\text{m}$ and $u_z = 0.47 \pm 0.17 \mu\text{m}$.

4.2.4 Histological Study

All tested and control samples were equilibrated in a 30% sucrose solution before sectioning using a Leica CM1950 cryostat (Leica, Bannockburn, IL). 100m thick longitudinal sections were serially collected and placed in wells. Depth of the section within the nerve was determined based on the distance from the exterior surface, regardless of nerve orientation

(top vs bottom). The collagen fibers were visualized via second harmonic generation (SHG) imaging using a Bruker Ultima Multi-photon confocal microscope with a Nikon LWD 16x water immersion objective (numerical aperture of 0.8) and PrairieView Software. A Coherent Cameleon Vision IR laser was tuned to a wavelength of 800nm and detection was performed using non-descanned PMT detectors. SHG signals were discriminated from background autofluorescence using a 460LP dichroic and 377/50nm bandpass filter, limiting detected signal to a range of 377-402nm. Collagen fiber angles were evaluated using a custom Matlab code [90, 101]. Fiber angles were normalized so that the mean fiber angle for each section was equal to zero (zero is the direction along the length of the nerve).

4.2.5 Statistical Analysis

A linear mixed model was used to analyze the compression tests data. Pressure level (0-40, and 40-80 mmHg), nerve side (left and right), nerve section (distal and proximal) and age group (piglet and pig) were considered as fixed effects while animal subjects were included as a random effect. Since the residuals of the strain data were not normally distributed, we used Box-Cox transformation to transform all data to normal [19]. After satisfying all requirements, we fitted the transformed data to a linear mixed model and utilized 4-way ANOVA to identify significant differences with an alpha level of 5% using a Bonferroni correction to adjust for multiple comparisons [96]. The histological study results were optimally binned using Sturges method [53] followed by Bartlett's test [104] to study homogeneity of variances for the distribution of collagen fibers orientation at 0 and 80 mmHg. Moreover, we employed a paired t-test to scrutinize the variation of the RLN diameter under compression for pig and piglets.

4.3 Results

3D Displacement field, strain components, and principal strains were computed for all samples (Figure 19). A significant main effect was identified for the animal age at the first

pressure increment (i.e., 0 to 40 mmHg) with the median and 95th percentile (%95) of the 1st principal strain (E_{ps1}). Figure 20A shows that the median of E_{ps1} for the left distal segment is significantly higher in pigs compared to piglets using a Bonferroni pairwise correction (p-value =0.004). Also, the median of E_{ps1} for the similar RLN segment was significantly larger at the first pressure increment compared to the second increment in pigs (p-value =0.018).

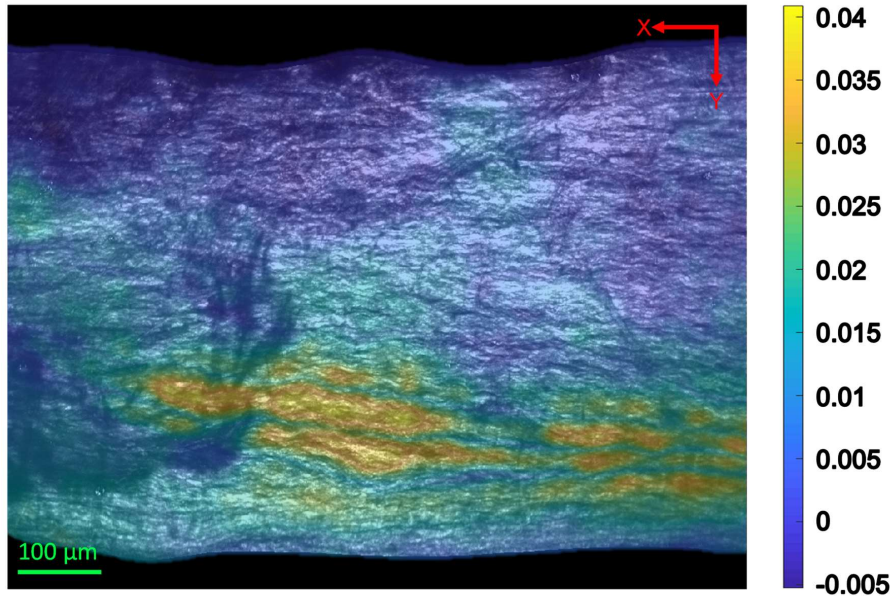


Figure 19: Strain component in the axial direction (E_{xx}) averaged through the thickness (z -axis) for the distal section of a right piglet RLN at the first pressure increment

Furthermore, as depicted in Figure 20B, a similar trend was observed in the %95 of the E_{ps1} . For the distal segment of the left RLN at the first pressure increment, %95 of E_{ps1} was significantly larger in pigs than piglets (p-value = 0.003). Pressure level was also significant

for the %95 of E_{ps1} in the left distal segment of the RLN. Figure 20B shows that within the pig group, %95 of E_{ps1} is larger at the first pressure increment compared to the second increment (p-value = 0.016). Although the statistical analysis did not show any significant differences in the principal direction across the study groups, it is noteworthy to mention that the average of the X component of the first principal direction was relatively smaller than the other two components.

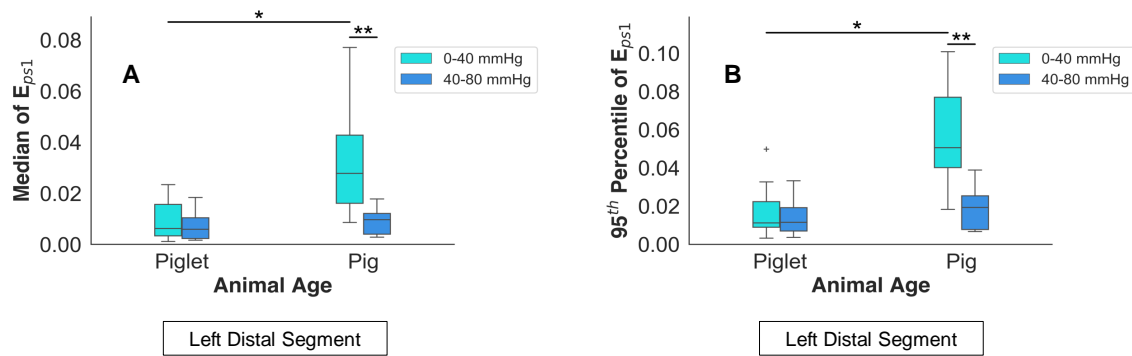


Figure 20: Strain metrics for the left distal segment of the RLN as a function of animal age and pressure level A) Median of the E_{ps1} was significantly higher in pigs compared to piglets at the first pressure increment. Also, it was higher in pig group at the first pressure increment compared to the second pressure increment. B) 95th percentile of the 1st principal strain showed a similar trend as the median of the E_{ps1} .

A significant main effect (p-value = 0.001) was identified for the animal age group at the second pressure step with the median of the transverse strain (E_{yy}) being larger in pig group than the piglets for the proximal section of the right RLN (Figure 21). Moreover, nerve side was a significant main effect for E_{yy} which was higher in the proximal section of the right pig RLN compared to the same segment of the pig left RLN at the second pressure level.

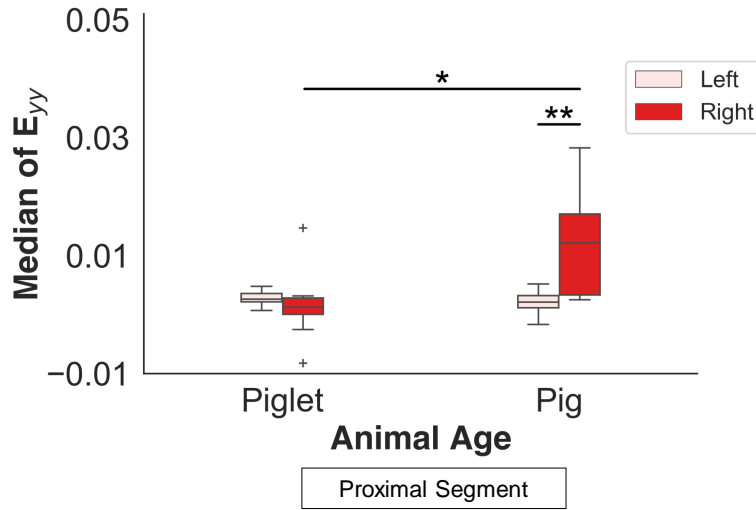


Figure 21: At the second pressure increment and for the proximal segment of RLN, the median of E_{yy} across the pig group was significantly larger than the left side. Also, it was greater in the pig right RLN compared to the right piglet RLN.

The histological studies illustrated that RLN in the pig group had a significant reduction in the nerve diameter following compression testing (p-value = 0.026). However, a comparison between experimental and control samples in the piglet group did not show any statistically significant difference in the RLN diameter. In addition, Bartlett's test showed that the variance of the collagen fiber distributions at 0 and 80 mmHg are not significantly different (Figure 22).

4.4 Discussion

The result of our study showed several differences in the porcine RLN biomechanical response across different study groups under compression. We showed that the transverse

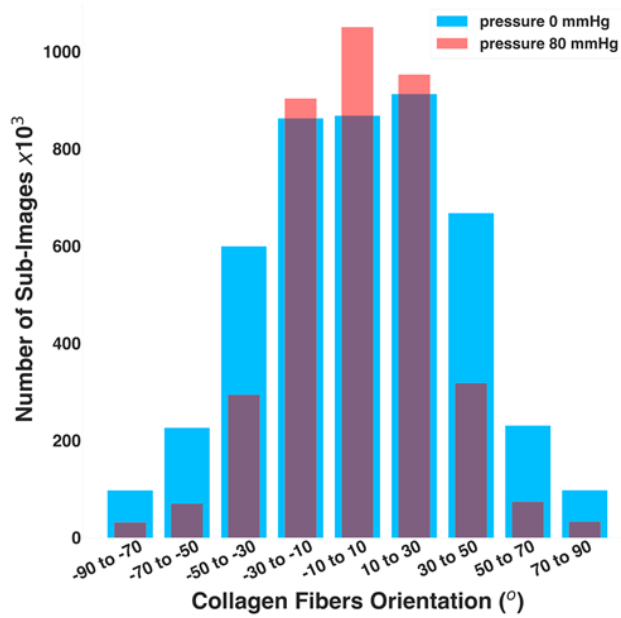


Figure 22: Distribution of the collagen fiber orientation at 0 and 80 mmHg

strain (E_{yy}) is significantly higher in the proximal section of the right RLN compared to the same segment of left RLN in the pig group. Differences in the RLN strain level stem from the fact that the microstructure and biomechanical properties of the RLN are a function of age and location in porcine. Williams et al. assessed microstructure and the biomechanical response of the porcine RLN using a uniaxial tension test. They demonstrated that the strain energy density is larger in the proximal segment of the left RLN compared to a similar segment at the right side [123]. Furthermore, Campbell et al. conducted a study on RLN composition and showed that the proximal segment of the pig right RLN exhibited more adipose and less collagen [21]. Higher strain level in the proximal segment of the right RLN could be attributed to the soft nature of adipose [6]. Furthermore, Sunderland hypothesized that there is an association between peripheral nerve biomechanical environment and connective tissue composition [113, 111, 114]. The proximal segment of the left RLN is stretched by the aortic arch and compressed against the pulmonary artery during each cardiac cycle.

As evident by the lower strain level in the left proximal RLN, our results are consistent with Sunderlands studies. The complex loading paradigm at the location of the left proximal RLN necessitates a stiffer material and consequently lower strain values to preserve axons.

Given the fact that the main proportion of the epineural collagen is oriented longitudinally in both left and right RLNs [123], some studies have shown that collagen contributes to the mechanical stiffness in the stretch and adipose preserve the axons under compression [62, 42, 112]. Similarly, our histological studies did not show any significant changes in collagen fiber orientation as a result of the RLN compression, which means collagen fibers did not contribute notably to the tissue biomechanical response under hydrostatic compression. In addition, the relatively small longitudinal component of the 1st principal strain direction suggests that axial tension was not mainly happening so collagen fibers should remain mostly unrecruited.

We demonstrated that the median of first principal strain (E_{ps1}) is significantly higher in pigs compared to piglets in the distal segment of the left RLN. Campbell et al. showed that the piglet epineurium is mainly consisted of collagen, while the pig epineurium comprised of collagen and adipose tissue [21]. Moreover, another study on the human sciatic nerve showed that the adipose content significantly increases with age [103]. Greater strain values in the pig group could ascribe to postnatal development of adipose in the pig RLN compared to the piglet.

Campbell et al. demonstrated that piglet RLN tissue appeared more homogeneous within and between the left and right sides compared to pigs. They showed that the proportion of the epineurium, perineurium, collagen, and adipose in piglet group is not varying with location (i.e., left or right, proximal or distal) [21]. Homogeneity of the RLN composition within the piglet group implies that the biomechanical properties of the RLN in piglet is not varying at different locations. Thus, the biomechanical response of the nerve (i.e., strain field) within the piglet group should not be a function of location. Consistent with the prior study, our analysis did not show any significant differences in the biomechanical response of the RLN under compression within the piglet group.

Although stretch related injuries are the most common peripheral nerve injury type [111], compression is considered to be another common cause for the nerve damage. Generally,

nerve compression does not involve a severe rupture or tearing similar to the stretch-induced injuries, yet the total loss of both motor and sensory function might be a viable consequence of the supraphysiological compression [20]. The most common mechanisms for the nerve damage under compression could be categorized into mechanical deformation and ischemia. Some studies have shown that in the short-term compression, ischemia plays a more important role in the nerve damage by affecting the large myelinated fibers [59]. In contrast, mechanical deformation is assumed to cause degenerative changes in the regions of the compressed nerve, which are less affected by ischemia [81, 82].

The cyclic deformation of the left RLN might be another contributor to the nerve damage. Watanabe et al. employed a rat forelimb model to study nerve injury as a result of continuous and repeated loading. They showed that under a continuous stretch applied to the nerve by a small load (i.e., 2N), no histological, electrophysiological or functional impairment was noted. In contrast, if a similar load is applied in a cyclic manner (60 to 120 times per hour), some significant differences were observed in the above parameters [120]. The above damage mechanism is important as the left RLN is continuously compressed and stretch in each cardiac cycle. As UVP is more prevalent across the elderly [24], a slightly higher level of compression or stretch applied by a hypercompliant aortic arch at each cardiac cycle for a long period might be a possible cause for the left RLN injury. Various animal models have been utilized to demonstrate the situation of clinical (i.e., chronic) nerve compression. It has been shown that nerve damage under chronic compression begins with the breakdown of the nerve blood barrier, fibrosis, and subperineurial edema at the early stages. In severe cases of injury, subsequent demyelination, and axonal degeneration may occur, which lead to permanent nerve damage [80, 29, 66]. Also, Rydevik et al. showed that supraphysiological external pressure could influence axonal transport and intraneural blood flow adversely [98]. In addition, external pressure between 20 to 30 mmHg has been shown to affect venular flow in the epineurium, which influences the nerve microenvironment adversely [26].

5.0 Discussion

In this chapter, a summary of the the findings has been presented. Also, Limitations, future direction and the final conclusion of the study were included.

5.1 Overview

In this dissertation, we investigated an association between the cardiovascular system and the onset and development of the iUVP. The close interaction between the left RLN and the aortic arch and the higher prevalence of the left-sided iUVP led us to focus on the role of the aortic arch biomechanics in development of the iUVP. We studied biomechanical behavior of the aortic arch in a group of iUVP subjects without any history of known causes of vocal fold paralysis. A group of age-gender matched subjects were also studied as the control group.

In the first step (chapter two), the compliance of the aortic arch for both study groups was measured. We utilized advanced image processing methods and compared normalized circumferential deformation of the aortic arch across different groups. In the second step (chapter three), the *in vivo* data was used to characterize the mechanical properties of the aortic arch. We employed an inverse finite element approach using an anisotropic material model to determine the constitutive parameter of the aortic arch wall. The last stage of this work was devoted to studying the microstructure of the RLN connective tissue. As the RLN connective tissues preserve the integrity of the axons in different loading conditions, we implemented mechanical testing to study the biomechanical behavior of the RLN in response to the hydrostatic compression (chapter four).

5.2 Summary of Results

5.2.1 Chapter 2: Compliance Variation Across iUVP Patients and Healthy Subjects

In chapter two, we calculated the diameter of the aortic arch using gated MRI data for ten subjects diagnosed with iUVP and ten age-gender matched controls. This information was later used to determine the compliance of the aortic arch. We demonstrated that the compliance of the aortic arch is greater in the iUVP group. It was also shown that the aortic arch compliance is decreasing with age. Furthermore, we showed that regardless of age, compliance is greater in the iUVP group compared to the controls. Additionally, we performed a separate statistical analysis and showed that the average of the aortic arch diameter change in the iUVP patients is significantly greater than the controls. We employed a 3-way ANOVA to study all the interaction between the main effects (i.e., age, gender, and disease) nevertheless; gender was not presented as one of the significant main effect for compliance.

As pressure pulse affects the aortic arch compliance greatly, we employed a 3-way ANOVA test to study the effect of age, gender, and disease on pressure pulse. Our statistical analysis showed that pressure pulse in middle age and old group is significantly higher than the young group.

Our findings suggest that the differences in the aortic arch compliance could be a potential cause for iUVP. A hypercompliant aortic arch could impose a supraphysiological level of compression and tension on the left RLN during each cardiac and lead to the RLN damage over time. As differences in the aortic arch compliance between iUVP subjects and controls might stem from the variation in the mechanical properties of the aortic arch, characterization of the aortic arch mechanical properties would lead us to understand the connection between the aortic arch biomechanical environment and RLN damage.

5.2.2 Chapter 3: Specific Aim 2 Determination of the Aortic Arch Mechanical Properties for iUVP Patients and Controls Using *in vivo* Data

We showed that the compliance of the aortic arch is a function of diseases. That means, the aortic arch is more compliant in iUVP patients, which eventually could impose higher level of compression and stretch on the nerve chronically. We utilized an inverse finite element approach to characterize the mechanical properties of the aortic wall, and we showed several differences across the study groups. Utilization of the hyperelastic anisotropic model enabled us to study different constituent of the aortic wall. Our study showed that C_{10} , K_1 , and K_2 are significantly smaller in iUVP patients within the old age group. We also showed that all the material parameters increase with age in both study groups. As C_{10} and K_1 contribute directly to the stiffness, decreased values of these parameters result in a more compliant aortic wall. We showed that differences in material properties of the aortic arch might be one potential cause for the higher compliance across the iUVP patients.

5.2.3 Chapter 4: Extracellular matrix deformations of the porcine recurrent laryngeal nerve in response to compression

In chapter two, we showed that the left RLN in iUVP patients is potentially experiencing a higher level of compression and tension as the aortic arch is hypercompliant in this group. As the RLN connective tissue plays a crucial role in the biomechanical response of the nerve, we sought to study the biomechanical response of the RLN connective tissue in response to mechanical compression. We employed a porcine model due to the similarity between porcine and humans for laryngeal innervation patterns, anatomy, and function. We determined the mechanical strain field in different segments (i.e., distal and proximal) of the left and right RLN. We showed that median of the first principal strain is greater in the distal segment of the right RLN compared to the same segment of the left side in pigs. For the same segment, we showed that the E_{ps1} in the first pressure step is greater in pigs compared to the piglets. Furthermore, 95th percentile of the E_{ps1} showed a similar trend. Interestingly, we showed that the transverse strain (E_{yy}) in the proximal segment of the left nerve is significantly smaller than the right nerve in pigs. In addition, E_{yy} in the proximal segment of the right

pig RLN is significantly greater than the same segment of the piglet group. We also did not observe any statistically significant difference between various segments of the piglet RLN.

The histological study showed that the nerve diameter was significantly decreased in response to compression. However, no significant change was observed in the piglet RLN due to hydrostatic compression. Lastly, We studied the collagen fiber alignment before and after compression, and our study did not show any significant change in the collagen fiber alignment in pigs.

Greater level of the mechanical strain in some of the RLN segments with higher adipose content confirms that adipose is mainly responsible for preserving the axons under compression. Moreover, the histological study suggests that collagen fibers remain unrecruited during compression, which confirms their minimal role in the biomechanical response of the RLN under compression. Our findings provided us with insightful information about the RLN response under compression. This information could be used later in a computational framework to predict potential nerve damage as a result of imposing a supraphysiological level of compression.

5.3 Limitation and Future Work

The work presented in this dissertation is an initial step toward to build computational and experimental frameworks to understand a potential etiology of iUVP. Based on the observations and results of this work, this section is devoted to proposing future direction.

Our mechanical testing (i.e., hydrostatic compression) showed that the biomechanical environment of the nerve could vastly affect the biomechanical response of the RLN. As the geometrical properties of the arch contribute to the tissue mechanical response, implementing an experiment in which a mock arch geometry is loading in a pulsatile manner and interacts with the RLN (excised from a pig) could provide us with invaluable information about RLN response under mechanical insult. The new 3D printing methods allow us to tune the mechanical properties of the mock aortic arch and create models with different level of compliance [73, 92, 17]. A peristaltic pump could be utilized to mimic the pulsatile nature

of the blood flow in the aorta. Also, the electrophysiological activity of the nerve could be monitored by performing compound action potential tests. Furthermore, this model will help us to study how adjustments in the pressure pulse or mechanical properties affect the RLN response. In addition, we can simulate some pathological conditions such as aneurysm using 3D printing and directly study the correlation of the RLN biomechanical response and aortic arch geometry.

As it was mentioned in chapter 4, hypoxia is a potential cause for the RLN damage under mechanical loading. Supraphysiological loads might block the blood flow in the RLN microvasculature and prevents oxygen and nutrition delivery to the tissue. Visualization of the nerve microvasculature would enable us to investigate the effect of the mechanical loading on the blood vessel network in the RLN. Several studies have proposed different methods for labeling the endothelial cells. An *in vivo* compression or stretch test prior to the nerve vasculature staining and fixing could be used to visualize the changes in the vasculature morphology. The results of this study can be later used to estimate a threshold for the RLN damage under mechanical loading. As it was mentioned in chapter 4, hypoxia is a potential cause for the RLN damage under mechanical loading. Supraphysiological loads might block the blood flow in the RLN microvasculature and prevents oxygen and nutrition delivery to the tissue. Visualization of the nerve microvasculature would enable us to investigate the effect of the mechanical loading on the blood vessel network in the RLN. Several studies have proposed different methods for labeling the blood vessels [93, 1]. An *in vivo* compression or stretch test prior to the nerve vasculature staining and fixing could be used to visualize the changes in the vasculature morphology. The results of this study can be later used to estimate a threshold for the RLN damage under mechanical loading.

There are also a few limitations associated with this study. In the finite element model, the thickness data was borrowed from the literature. Moreover, we used the blood pressure measurements collected by regular pressure cuff from the brachial artery. This data can significantly improve the results. It is possible to collect thickness data using a high-resolution echo tracking device. Also, pressure can be measured using an applanation tonometer [70]. The patient-specific thickness and pressure data can significantly improve the accuracy of the results. In addition, including the opening angle to account for the residual stress would

result in a more comprehensive computational model. Another limitation of this work was the depth limitation in multiphoton imaging of the nerve. SHG imaging enabled us to study the microstructure of RLN connective tissue however depth was limited to 250 μm . Using other imaging methods such as phase contrast μCT could be considered as an alternative approach to visualize the entire nerve volume.

5.4 Dissertation Conclusions

In this dissertation, we studied the interaction of the aortic arch with the left RLN to better understand any potential cause of the vocal fold paralysis as it relates to the biomechanics of the aortic arch. Several studies have shown that there is a link between some cardiovascular diseases such as aneurysm and the neurogenic UVP. Given the course of the left RLN in the thorax, we hypothesized that creating an unfavorable biomechanical environment by the RLN adjacent tissues such as the aortic arch might be a cause for the nerve damage. We showed that arch compliance is significantly different across iUVP patients and control. Our findings confirm the pivotal role of the aortic arch biomechanics in the onset of iUVP. As iUVP is more prevalent in the age 50, and above, chronic nerve damage due to a higher level of compression and stretch imposed by the hypercompliant arch could be a potential cause for the RLN damage. We also designed a computational framework to inversely calculate the mechanical properties of the aortic arch using an anisotropic hyperelastic material model. Consistent with our findings on the arch compliance, we showed that the material properties are different in iUVP patients compared to the controls. In this work, we successfully utilized *in vivo* data and determined the constitutive parameters. The *in vivo* characterization shows the material behavior more accurately as the tissue should not be detached from its native environment for mechanical testing. Finally, we studied the RLN behavior as a function of the age and anatomical location in response to compression. Our results confirmed that the RLN connective tissue develops in response to the biomechanical environment forces. The results prior study improved our understanding of the tissue behavior under mechanical insult. The results of the mechanical test suggested that adipose is the

main contributor in preserving axons under compression. Although this study introduced a new possible etiology for iUVP, some complementary studies on the aortic arch geometrical and morphological properties and RLN microvasculature would provide us with more significant information to better evaluate the role of the aortic arch biomechanics in the onset and development of the iUVP.

Bibliography

- [1] direct labeling and visualization of blood vessels with lipophilic carbocyanine dye Dil - Google Search.
- [2] Mackinnon, S.E., Pathophysiology of nerve compression. *Hand clinics*, 2002. 18(2): p. 231-241. - Google Search.
- [3] Seddon, H., A classification of nerve injuries. *British medical journal*, 1942. 2(4260): p. 237 - Google Search.
- [4] K. Z. Abd-Elmoniem, M. Stuber, and J. L. Prince. Direct three-dimensional myocardial strain tensor quantification and tracking using zHARP. *Medical Image Analysis*, 12(6):778–786, December 2008.
- [5] M. J. Alexander, J. M. Barkmeier-Kraemer, and J. P. V. Geest. Biomechanical Properties of Recurrent Laryngeal Nerve in the Piglet. *Annals of Biomedical Engineering*, 38(8):2553–2562, August 2010.
- [6] Nadia Alkhouli, Jessica Mansfield, Ellen Green, James Bell, Beatrice Knight, Neil Liversedge, Ji Chung Tham, Richard Welbourn, Angela C. Shore, and Katarina Kos. The mechanical properties of human adipose tissues and their relationships to the structure and composition of the extracellular matrix. *American Journal of Physiology-Endocrinology and Metabolism*, 305(12):E1427–E1435, 2013.
- [7] M. R. Amin and J. A. Koufman. Vagal neuropathy after upper respiratory infection: a viral etiology? *Am J Otolaryngol*, 22(4):251–6, August 2001.
- [8] L. Antiga, B. Ene-Iordache, and A. Remuzzi. Computational geometry for patient-specific reconstruction and meshing of blood vessels from MR and CT angiography. *IEEE Trans Med Imaging*, 22(5):674–84, May 2003.
- [9] L. Antiga, M. Piccinelli, L. Botti, B. Ene-Iordache, A. Remuzzi, and D. A. Steinman. An image-based modeling framework for patient-specific computational hemodynamics. *Med Biol Eng Comput*, 46(11):1097–112, November 2008.

- [10] A. P. Avolio, L. M. Van Bortel, P. Boutouyrie, J. R. Cockcroft, C. M. McEniery, A. D. Protogerou, M. J. Roman, M. E. Safar, P. Segers, and H. Smulyan. Role of pulse pressure amplification in arterial hypertension: experts' opinion and review of the data. *Hypertension*, 54(2):375–83, August 2009.
- [11] A. Ayyalasomayajula, A. Polk, A. Basudhar, S. Missoum, L. Nissim, and J. P. Vande Geest. Three dimensional active contours for the reconstruction of abdominal aortic aneurysms. *Ann Biomed Eng*, 38(1):164–76, January 2010.
- [12] Julie M. Barkmeier and Erich S. Luschei. Quantitative analysis of the anatomy of the epineurium of the canine recurrent laryngeal nerve. *The Journal of Anatomy*, 196(1):85–101, 2000.
- [13] R. Behkam, K. E. Roberts, A. J. Bierhals, M. E. Jacobs, J. D. Edgar, R. C. Paniello, G. Woodson, J. P. Vande Geest, and J. M. Barkmeier-Kraemer. Aortic arch compliance and idiopathic unilateral vocal fold paralysis. *J Appl Physiol (1985)*, 123(2):303–309, August 2017.
- [14] Reza Behkam, Hirut G. Kollach, Anirban Jana, Amy Hill, Forest Danford, Stephen Howerton, Sundaresh Ram, Jeffrey J. Rodriguez, Urs Utzinger, and Christopher A. Girkin. Racioethnic differences in the biomechanical response of the lamina cribrosa. *Acta biomaterialia*, 88:131–140, 2019.
- [15] C. J. Beller, M. R. Labrosse, M. J. Thubrikar, and F. Robicsek. Role of aortic root motion in the pathogenesis of aortic dissection. *Circulation*, 109(6):763–9, February 2004.
- [16] H. Berry and R. L. Blair. Isolated vagus nerve palsy and vagal mononeuritis. *Arch Otolaryngol*, 106(6):333–8, June 1980.
- [17] Giovanni Biglino, Claudio Capelli, Andrew M. Taylor, and Silvia Schievano. 3d printing cardiovascular anatomy: a single-centre experience. *New Trends in 3D Printing*, 2016.
- [18] J. N. Blau and R. Kapadia. Idiopathic palsy of the recurrent laryngeal nerve: a transient cranial mononeuropathy. *Br Med J*, 4(5835):259–61, November 1972.
- [19] George EP Box and David R. Cox. An analysis of transformations. *Journal of the Royal Statistical Society: Series B (Methodological)*, 26(2):211–243, 1964.

- [20] Mark G. Burnett and Eric L. Zager. Pathophysiology of peripheral nerve injury: a brief review. *Neurosurgical focus*, 16(5):1–7, 2004.
- [21] E. O. Campbell, R. A. Samlan, N. T. McMullen, S. Cook, S. Smiley-Jewell, and J. Barkmeier-Kraemer. Developmental changes in the connective tissues of the porcine recurrent laryngeal nerve. *J Anat*, 222(6):625–33, June 2013.
- [22] T. F. Chan and L. A. Vese. Active contours without edges. *Ieee Transactions on Image Processing*, 10(2):266–277, February 2001.
- [23] D. W. Chen, A. Young, D. T. Donovan, and J. Ongkasuwan. Routine Computed Tomography in the Evaluation of Vocal Fold Movement Impairment without an Apparent Cause. *Otolaryngology-Head and Neck Surgery*, 152(2):308–313, February 2015.
- [24] Suzanne M. Coyle, Barbara D. Weinrich, and Joseph C. Stemple. Shifts in relative prevalence of laryngeal pathology in a treatment-seeking population. *Journal of Voice*, 15(3):424–440, 2001.
- [25] Kostadin Dabov, Alessandro Foi, Vladimir Katkovnik, and Karen Egiazarian. Image denoising with block-matching and 3d filtering. volume 6064, page 606414. International Society for Optics and Photonics, 2006.
- [26] Lars B. Dahlin and W. Graham McLean. Effects of graded experimental compression on slow and fast axonal transport in rabbit vagus nerve. *Journal of the neurological sciences*, 72(1):19–30, 1986.
- [27] Jonathan RS Day and Robin K. %J The Annals of thoracic surgery Walesby. A spontaneous ductal aneurysm presenting with left recurrent laryngeal nerve palsy. 72(2):608–609, 2001.
- [28] H. H. Dedo. The paralyzed larynx: an electromyographic study in dogs and humans. *Laryngoscope*, 80(10):1455–517, October 1970.
- [29] A. Lee Dellon and Susan E. Mackinnon. Chronic nerve compression model for the double crush hypothesis. *Annals of plastic surgery*, 26(3):259–264, 1991.
- [30] David A. Dolowitz and CS %J The American journal of medicine Lewis. Left vocal cord paralysis associated with cardiac disease. 4(6):856–862, 1948.

- [31] P. J. Driscoll, M. A. Glasby, and G. M. Lawson. An in vivo study of peripheral nerves in continuity: biomechanical and physiological responses to elongation. *Journal of Orthopaedic Research*, 20(2):370–375, March 2002.
- [32] I. D. Duncan, I. R. Griffiths, A. McQueen, and G. O. Baker. The pathology of equine laryngeal hemiplegia. *Acta Neuropathol*, 27(4):337–48, April 1974.
- [33] V. Dupuch, N. Saroul, C. Aumeran, R. Pastourel, T. Mom, and L. Gilain. Bilateral vocal cord abductor paralysis associated with primary herpes simplex infection: a case report. *Eur Ann Otorhinolaryngol Head Neck Dis*, 129(5):272–4, October 2012.
- [34] LM %J Journal of the Egyptian Medical Association El-Ahmady. Left vocal cord paralysis in bilharzial pulmonary aneurysm.(Case report.). 57(5/6):232–236, 1974.
- [35] F. Faul, E. Erdfelder, A. G. Lang, and A. Buchner. G*Power 3: a flexible statistical power analysis program for the social, behavioral, and biomedical sciences. *Behav Res Methods*, 39(2):175–91, May 2007.
- [36] R. H. Flowers and D. S. Kernodle. Vagal mononeuritis caused by herpes simplex virus: association with unilateral vocal cord paralysis. *Am J Med*, 88(6):686–8, June 1990.
- [37] T. C. Gasser, R. W. Ogden, and G. A. Holzapfel. Hyperelastic modelling of arterial layers with distributed collagen fibre orientations. *J R Soc Interface*, 3(6):15–35, February 2006.
- [38] M. Gaubitz. Epidemiology of connective tissue disorders. *Rheumatology*, 45(suppl.3):iii3–iii4, 2006.
- [39] Jonathan P. Vande Geest, Michael S. Sacks, and David A. Vorp. Age dependency of the biaxial biomechanical behavior of human abdominal aorta. *Journal of biomechanical engineering*, 126(6):815–822, 2004.
- [40] Jonathan P. Vande Geest, Michael S. Sacks, and David A. Vorp. The effects of aneurysm on the biaxial mechanical behavior of human abdominal aorta. *Journal of biomechanics*, 39(7):1324–1334, 2006.
- [41] R. Gupta, N. Nassiri, A. Hazel, M. Bathen, and T. Mozaffar. Chronic nerve compression alters Schwann cell myelin architecture in a murine model. *Muscle Nerve*, 45(2):231–41, February 2012.

- [42] Jan Haftek. Stretch injury of peripheral nerve: acute effects of stretching on rabbit nerve. *The Journal of bone and joint surgery. British volume*, 52(2):354–365, 1970.
- [43] Joseph V. Hajnal and Derek LG Hill. *Medical image registration*. CRC press, 2001.
- [44] J. M. Haller, M. Iwanik, and F. H. Shen. Clinically relevant anatomy of recurrent laryngeal nerve. *Spine*, 37(2):97–100, January 2012.
- [45] D. Haskett, G. Johnson, A. F. Zhou, U. Utzinger, and J. Vande Geest. Microstructural and biomechanical alterations of the human aorta as a function of age and location. *Biomechanics and Modeling in Mechanobiology*, 9(6):725–736, December 2010.
- [46] R. F. Heitmiller, E. Tseng, and B. Jones. Prevalence of aspiration and laryngeal penetration in patients with unilateral vocal fold motion impairment. *Dysphagia*, 15(4):184–187, 2000.
- [47] Stacey S. Hickson, Mark Butlin, Martin Graves, Valentina Taviani, Alberto P. Avolio, Carmel M. McEniery, and Ian B. Wilkinson. The relationship of age with regional aortic stiffness and diameter. *JACC: Cardiovascular Imaging*, 3(12):1247–1255, 2010.
- [48] R. P. Hillstrom, A. M. Cohn, and K. A. Mccarroll. Vocal Cord Paralysis Resulting from Neck Injections in the Intravenous Drug-Use Population. *Laryngoscope*, 100(5):503–506, May 1990.
- [49] Gerhard A. Holzapfel, Thomas C. Gasser, Ray W. %J Journal of elasticity Ogden, and the physical science of solids. A new constitutive framework for arterial wall mechanics and a comparative study of material models. 61(1-3):1–48, 2000.
- [50] Gerhard A. Holzapfel, Thomas C. %J Computer methods in applied mechanics Gasser, and engineering. A viscoelastic model for fiber-reinforced composites at finite strains: Continuum basis, computational aspects and applications. 190(34):4379–4403, 2001.
- [51] Jay D. Humphrey. *Cardiovascular solid mechanics*. Springer New York, New York, NY, 2002.
- [52] Yutaka Imauchi, Yukitomo Urata, and Kazuya Abe. Left vocal cord paralysis in cases of systemic lupus erythematosus. *ORL*, 63(1):53–55, 2001.

- [53] B. C. Kang, J. L. Roh, J. H. Lee, J. H. Jung, S. H. Choi, S. Y. Nam, and S. Y. Kim. Usefulness of computed tomography in the etiologic evaluation of adult unilateral vocal fold paralysis. *World J Surg*, 37(6):1236–40, June 2013.
- [54] L. N. Kelchner, J. C. Stemple, E. Gerdeman, W. Le Borgne, and S. Adam. Etiology, pathophysiology, treatment choices, and voice results for unilateral adductor vocal fold paralysis: a 3-year retrospective. *J Voice*, 13(4):592–601, December 1999.
- [55] D.-J. Kroon. Image and Point based Registration. 2016.
- [56] R. M. Lang, B. P. Cholley, C. Korcarz, R. H. Marcus, and S. G. Shroff. Measurement of regional elastic properties of the human aorta. A new application of transesophageal echocardiography with automated border detection and calibrated subclavian pulse tracings. *Circulation*, 90(4):1875–82, October 1994.
- [57] T. Lanne, H. Stale, H. Bengtsson, D. Gustafsson, D. Bergqvist, B. Sonesson, H. Lecerof, and P. Dahl. Noninvasive measurement of diameter changes in the distal abdominal aorta in man. *Ultrasound Med Biol*, 18(5):451–7, 1992.
- [58] Hava Lester and Simon R. %J Pattern recognition Arridge. A survey of hierarchical non-linear medical image registration. 32(1):129–149, 1999.
- [59] Pickering GW Lewis T. Centripetal paralysis arising out of arrested bloodflow to the limb. *Heart*, 16:1–32, 1931.
- [60] A. E. Li, I. Kamel, F. Rando, M. Anderson, B. Kumbasar, J. A. C. Lima, and D. A. Bluemke. Using MRI to assess aortic wall thickness in the multiethnic study of atherosclerosis: Distribution by race, sex, and age. *American Journal of Roentgenology*, 182(3):593–597, March 2004.
- [61] J. Li and R. Shi. Stretch-induced nerve conduction deficits in guinea pig ex vivo nerve. *J Biomech*, 40(3):569–78, 2007.
- [62] C. T. Liu, C. E. Benda, and F. H. Lewey. Tensile strength of human nerves: an experimental physical and histologic study. *Archives of Neurology & Psychiatry*, 59(3):322–336, 1948.
- [63] Minliang Liu, Liang Liang, and Wei Sun. Estimation of in vivo constitutive parameters of the aortic wall using a machine learning approach. *Computer methods in applied mechanics and engineering*, 347:201–217, 2019.

- [64] S. Loughran, C. Alves, and F. B. MacGregor. Current aetiology of unilateral vocal fold paralysis in a teaching hospital in the West of Scotland. *J Laryngol Otol*, 116(11):907–10, November 2002.
- [65] G. Lundborg, R. Myers, and H. Powell. Nerve Compression Injury and Increased Endoneurial Fluid Pressure - a Miniature Compartment Syndrome. *Journal of Neurology Neurosurgery and Psychiatry*, 46(12):1119–1124, 1983.
- [66] Susan E. Mackinnon, A. Lee Dellon, Alan R. Hudson, and Daniel A. Hunter. A primate model for chronic nerve compression. *Journal of reconstructive microsurgery*, 1(03):185–194, 1985.
- [67] JB Antoine Maintz and Max A. %J Medical image analysis Viergever. A survey of medical image registration. 2(1):1–36, 1998.
- [68] Ashkan A. Malayeri, Shunsuke Natori, Hossein Bahrami, Alain G. Bertoni, Richard Kronmal, Joo AC Lima, and David A. Bluemke. Relation of aortic wall thickness and distensibility to cardiovascular risk factors (from the Multi-Ethnic Study of Atherosclerosis [MESA]). *The American journal of cardiology*, 102(4):491–496, 2008.
- [69] I. Masson, P. Boutouyrie, S. Laurent, J. D. Humphrey, and M. Zidi. Characterization of arterial wall mechanical behavior and stresses from human clinical data. *J Biomech*, 41(12):2618–27, August 2008.
- [70] Ingrid Masson, Hlne Beaussier, Pierre Boutouyrie, Stphane Laurent, Jay D. Humphrey, and Mustapha Zidi. Carotid artery mechanical properties and stresses quantified using in vivo data from normotensive and hypertensive humans. *Biomechanics and Modeling in Mechanobiology*, 10(6):867–882, 2011.
- [71] C. M. McEniery, B. McDonnell, M. Munnery, S. M. Wallace, C. V. Rowe, J. R. Cockcroft, I. B. Wilkinson, and Anglo-Cardiff Collaborative Tr. Central pressure: Variability and impact of cardiovascular risk factors - The Anglo-Cardiff Collaborative Trial II. *Hypertension*, 51(6):1476–1482, June 2008.
- [72] VICTOR A. McKusICK. The cardiovascular aspects of Marfan’s syndrome: a heritable disorder of connective tissue. *Circulation*, 11(3):321–342, 1955.
- [73] Karen M. Meess, Richard L. Izzo, Maciej L. Dryjski, Richard E. Curl, Linda M. Harris, Michael Springer, Adnan H. Siddiqui, Stephen Rudin, and Ciprian N. Ionita. 3d printed abdominal aortic aneurysm phantom for image guided surgical planning

with a patient specific fenestrated endovascular graft system. In *Medical Imaging 2017: Imaging Informatics for Healthcare, Research, and Applications*, volume 10138, page 101380P. International Society for Optics and Photonics, 2017.

- [74] R. M. Menorca, T. S. Fussell, and J. C. Elfar. Nerve physiology: mechanisms of injury and recovery. *Hand Clin*, 29(3):317–30, August 2013.
- [75] Ashkan Monfared, Goutham Gorti, and Daniel %J The Laryngoscope Kim. Microsurgical anatomy of the laryngeal nerves as related to thyroid surgery. 112(2):386–392, 2002.
- [76] L. Mu and S. Yang. An experimental study on the laryngeal electromyography and visual observations in varying types of surgical injuries to the unilateral recurrent laryngeal nerve in the neck. *Laryngoscope*, 101(7 Pt 1):699–708, July 1991.
- [77] L. C. Mu and S. Yang. An Experimental-Study on the Laryngeal Electromyography and Visual Observations in Varying Types of Surgical Injuries to the Unilateral Recurrent Laryngeal Nerve in the Neck. *Laryngoscope*, 101(7):699–708, July 1991.
- [78] S. K. Mulpuru, B. C. Vasavada, G. K. Pudukollu, and A. G. Patel. Cardiovascular syndrome: a systematic review. *Heart Lung Circ*, 17(1):1–4, February 2008.
- [79] Katsurni Murata, T. Motayama, and C. %J Atherosclerosis Kotake. Collagen types in various layers of the human aorta and their changes with the atherosclerotic process. 60(3):251–262, 1986.
- [80] J. P. O’Brien, S. E. Mackinnon, A. R. MacLean, A. R. Hudson, A. L. Dellon, and D. A. Hunter. A model of chronic nerve compression in the rat. *Annals of plastic surgery*, 19(5):430–435, 1987.
- [81] J. Ochoa, G. Danta, T. J. Fowler, and R. W. Gilliatt. Nature of the nerve lesion caused by a pneumatic tourniquet. *Nature*, 233(5317):265, 1971.
- [82] J. Ochoa, T. J. Fowler, and Roger W. Gilliatt. Anatomical changes in peripheral nerves compressed by a pneumatic tourniquet. *Journal of Anatomy*, 113(Pt 3):433, 1972.
- [83] N. Ortner. Recurrenslahmung bei mitral stenose. *Wien Klin Wochenschr*, 10:753–5, 1897.

- [84] X. Pennec, P. Cachier, and N. Ayache. Understanding the "Demon's Algorithm": 3d non-rigid registration by gradient descent. *Medical Image Computing and Computer-Assisted Intervention, Miccai'99, Proceedings*, 1679:597–605, 1999.
- [85] Alan %J Neurons Peters and their supporting cells. The fine structure of the nervous system. 1970.
- [86] Jude M. Phillip, Ivie Aifuwa, Jeremy Walston, and Denis Wirtz. The mechanobiology of aging. *Annual review of biomedical engineering*, 17:113–141, 2015.
- [87] M. Piccinelli, A. Veneziani, D. A. Steinman, A. Remuzzi, and L. Antiga. A framework for geometric analysis of vascular structures: application to cerebral aneurysms. *IEEE Trans Med Imaging*, 28(8):1141–55, August 2009.
- [88] A. Pou and R. L. Carrau. Bilateral abductor vocal cord paralysis in association with herpes simplex infection: a case report. *Am J Otolaryngol*, 16(3):216–9, June 1995.
- [89] V. Pressler, JJ %J The Journal of thoracic McNamara, and cardiovascular surgery. Aneurysm of the thoracic aorta. Review of 260 cases. 89(1):50–54, 1985.
- [90] Sundaresh Ram, Forest Danford, Stephen Howerton, Jeffrey J. Rodriguez, and Jonathan P. Vande Geest. Three-dimensional segmentation of the ex-vivo anterior lamina cribrosa from second-harmonic imaging microscopy. *IEEE Transactions on Biomedical Engineering*, 65(7):1617–1629, 2017.
- [91] D. Rimon, L. Cohen, and J. Rosenfeld. Thrombosed giant left atrium mimicking a mediastinal tumor. *Chest*, 71(3):406–8, March 1977.
- [92] Beth Ripley, Tatiana Kelil, Michael K. Cheezum, Alexandra Goncalves, Marcelo F. Di Carli, Frank J. Rybicki, Mike Steigner, Dimitrios Mitsouras, and Ron Blankstein. 3d printing based on cardiac CT assists anatomic visualization prior to transcatheter aortic valve replacement. *Journal of cardiovascular computed tomography*, 10(1):28–36, 2016.
- [93] Richard T. Robertson, Samantha T. Levine, Sherry M. Haynes, Paula Gutierrez, Janie L. Baratta, Zhiqun Tan, and Kenneth J. Longmuir. Use of labeled tomato lectin for imaging vasculature structures. *Histochemistry and Cell Biology*, 143(2):225–234, February 2015.

- [94] Laura H. Swibel Rosenthal, Michael S. Benninger, and Robert H. %J The Laryngoscope Deeb. Vocal fold immobility: a longitudinal analysis of etiology over 20 years. 117(10):1864–1870, 2007.
- [95] Tania Rozario and Douglas W. DeSimone. The extracellular matrix in development and morphogenesis: a dynamic view. *Developmental biology*, 341(1):126–140, 2010.
- [96] RStudio. RStudio: Integrated Development Environment for R. 2018.
- [97] F. Rubens, W. Goldstein, N. Hickey, C. Dennie, and W. Keon. Hoarseness secondary to left atrial myxoma. *Chest*, 95(5):1139–40, May 1989.
- [98] B. Rydevik, G. Lundborg, and U. Bagge. Effects of graded compression on intraneural blood flow: An in vivo study on rabbit tibial nerve. *The Journal of hand surgery*, 6(1):3–12, 1981.
- [99] B. Rylski, B. Desjardins, W. Moser, J. E. Bavaria, and R. K. Milewski. Gender-related changes in aortic geometry throughout life. *Eur J Cardiothorac Surg*, 45(5):805–11, May 2014.
- [100] Michael S. Sacks and Wei Sun. Multiaxial mechanical behavior of biological materials. *Annual review of biomedical engineering*, 5(1):251–284, 2003.
- [101] Edward A. Sander and Victor H. Barocas. Comparison of 2d fiber network orientation measurement methods. *Journal of Biomedical Materials Research Part A: An Official Journal of The Society for Biomaterials, The Japanese Society for Biomaterials, and The Australian Society for Biomaterials and the Korean Society for Biomaterials*, 88(2):322–331, 2009.
- [102] Yuhui Shi and Russell C. Eberhart. Empirical study of particle swarm optimization. volume 3, pages 1945–1950. IEEE, 1999.
- [103] Ugrenovic Z. Sladjana, Jovanovic D. Ivan, and Stefanovi D. Bratislav. Microanatomical structure of the human sciatic nerve. *Surgical and Radiologic Anatomy*, 30(8):619–626, 2008.
- [104] George W. Snedecor and William G. Cochran. Statistical Methods, eight edition. *Iowa state University press, Ames, Iowa*, 1989.

- [105] Emily A. Spataro, David J. Grindler, and Randal C. Paniello. Etiology and time to presentation of unilateral vocal fold paralysis. *Otolaryngology–Head and Neck Surgery*, 151(2):286–293, 2014.
- [106] M. M. Stecker, K. Baylor, J. Wolfe, and M. Stevenson. Acute nerve stretch and the compound motor action potential. *J Brachial Plex Peripher Nerve Inj*, 6(1):4, 2011.
- [107] N. P. Steele and D. Myssiorek. West Nile virus induced vocal fold paralysis. *Laryngoscope*, 116(3):494–6, March 2006.
- [108] C. Stefanadis, C. Stratos, C. Vlachopoulos, S. Marakas, H. Boudoulas, I. Kallikazaros, E. Tsiamis, K. Toutouzas, L. Sioros, and P. Toutouzas. Pressure-diameter relation of the human aorta. A new method of determination by the application of a special ultrasonic dimension catheter. *Circulation*, 92(8):2210–9, October 1995.
- [109] H. H. Stocker and H. T. Enterline. Cardio-vocal syndrome: laryngeal paralysis in intrinsic heart disease. *Am Heart J*, 56(1):51–9, July 1958.
- [110] L. Sulica. The natural history of idiopathic unilateral vocal fold paralysis: evidence and problems. *Laryngoscope*, 118(7):1303–7, July 2008.
- [111] Sir Sydney %J Muscle Sunderland and Nerve: Official Journal of the American Association of Electrodiagnostic Medicine. The anatomy and physiology of nerve injury. 13(9):771–784, 1990.
- [112] SYDNEY SUNDERLAND. The adipose tissue of peripheral nerves. *Brain*, 68(2):118–122, 1945.
- [113] Sydney %J Brain Sunderland. The connective tissues of peripheral nerves. 88(4):841–854, 1965.
- [114] Sydney %J Neurosurgery Sunderland. Anatomical features of nerve trunks in relation to nerve injury and nerve repair. 17(CN_suppl_1):38–62, 1970.
- [115] P. Tewari and S. K. Aggarwal. Combined left-sided recurrent laryngeal and phrenic nerve palsy after coronary artery operation. *Annals of Thoracic Surgery*, 61(6):1721–1722, June 1996.

- [116] J.-P. Thirion. Image matching as a diffusion process: an analogy with Maxwell's demons. *Medical image analysis*, 2(3):243–260, 1998.
- [117] PK %J Journal of anatomy Thomas. The connective tissue of peripheral nerve: an electron microscope study. 97(Pt 1):35, 1963.
- [118] Alkiviadis Tsamis, Jeffrey T. Krawiec, and David A. %J Journal of the Royal Society Interface Vorp. Elastin and collagen fibre microstructure of the human aorta in ageing and disease: a review. 10(83):20121004, 2013.
- [119] M. E. Walsh, L. B. Sloane, K. E. Fischer, S. N. Austad, A. Richardson, and H. Van Remmen. Use of Nerve Conduction Velocity to Assess Peripheral Nerve Health in Aging Mice. *Journals of Gerontology Series a-Biological Sciences and Medical Sciences*, 70(11):1312–1319, November 2015.
- [120] Mitsunobu Watanabe, Makio Yamaga, Teiji Kato, Junji Ide, Toshio Kitamura, and Katsumasa Takagi. The implication of repeated versus continuous strain on nerve function in a rat forelimb model. *The Journal of hand surgery*, 26(4):663–669, 2001.
- [121] S. G. Waxman. Determinants of Conduction-Velocity in Myelinated Nerve-Fibers. *Muscle Nerve*, 3(2):141–150, 1980.
- [122] M. J. Williams, A. Ayylasomayaajula, R. Behkam, A. J. Bierhals, M. E. Jacobs, J. D. Edgar, R. C. Paniello, J. M. Barkmeier-Kraemer, and J. P. Vande Geest. A computational study of the role of the aortic arch in idiopathic unilateral vocal-fold paralysis. *J Appl Physiol*, 118(4):465–74, February 2015.
- [123] M. J. Williams, U. Utzinger, J. M. Barkmeier-Kraemer, and J. P. Vande Geest. Differences in the Microstructure and Biomechanical Properties of the Recurrent Laryngeal Nerve as a Function of Age and Location. *Journal of Biomechanical Engineering-Transactions of the Asme*, 136(8), August 2014.
- [124] Andreas Wittek, Wojciech Derwich, Konstantinos Karatolios, Claus Peter Fritzen, Sebastian Vogt, Thomas Schmitz-Rixen, and Christopher Blase. A finite element updating approach for identification of the anisotropic hyperelastic properties of normal and diseased aortic walls from 4d ultrasound strain imaging. *Journal of the mechanical behavior of biomedical materials*, 58:122–138, 2016.
- [125] Andreas Wittek, Konstantinos Karatolios, Claus-Peter Fritzen, Jrgen Bereiter-Hahn, Bernhard Schieffer, Rainer Moosdorf, Sebastian Vogt, and Christopher Blase. Cyclic

three-dimensional wall motion of the human ascending and abdominal aorta characterized by time-resolved three-dimensional ultrasound speckle tracking. *Biomechanics and Modeling in Mechanobiology*, 15(5):1375–1388, 2016.

- [126] Rose S. Wong, Fabrizio M. Follis, Bruce K. Shively, and Jorge A. Wernly. Osteogenesis imperfecta and cardiovascular diseases. *The Annals of thoracic surgery*, 60(5):1439–1443, 1995.
- [127] J. Zhou and Y. C. Fung. The degree of nonlinearity and anisotropy of blood vessel elasticity. *Proceedings of the National Academy of Sciences*, 94(26):14255–14260, 1997.